A&A 664, A196 (2022)
https://doi.org/10.1051/0004-6361/202243604

Astronomy & Astrophysics

Euclid preparation

XX. The Complete Calibration of the Color–Redshift Relation survey: LBT observations and data release⋆

Euclid Collaboration: R. Saglia[1,2], S. De Nicola[1], M. Fabricius[1], V. Guglielmo[3], J. Snigula[1], R. Zöller[1,2], R. Bender[1,2], J. Heidt[4], D. Masters[5], D. Stern[6], S. Paltani[7], A. Amara[8], N. Auricchio[3], M. Baldi[9,3,10], C. Bodendorf[1], D. Bonino[11], E. Branchini[12,13], M. Brescia[14], J. Brinchmann[15], S. Camera[16,17,11], V. Capobianco[11], C. Carbone[18], J. Carretero[19,20], M. Castellano[21], S. Cavuoti[14,22,23], R. Cledassou[24], G. Congedo[25], C. J. Conselice[26], L. Conversi[27,28], Y. Copin[29], L. Corcione[11], F. Courbin[30], M. Cropper[31], A. Da Silva[32,33], H. Degaudenzi[7], M. Douspis[34], F. Dubath[7], C. A. J. Duncan[35], X. Dupac[27], S. Dusini[36], S. Farrens[37], M. Frailis[38], E. Franceschi[3], S. Galeotta[38], B. Garilli[18], W. Gillard[39], B. Gillis[25], C. Giocoli[40,41], A. Grazian[42], F. Grupp[1,2], S. V. H. Haugan[43], H. Hoekstra[44], W. Holmes[6], F. Hormuth[45], A. Hornstrup[46], K. Jahnke[47], M. Kümmel[2], S. Kermiche[39], A. Kiessling[6], M. Kunz[48], H. Kurki-Suonio[49], R. Laureijs[50], S. Ligori[11], P. B. Lilje[43], I. Lloro[51], E. Maiorano[3], O. Marggraf[52], K. Markovic[6], F. Marulli[53,3,10], R. Massey[54], H. J. McCracken[55], M. Melchior[56], G. Meylan[30], M. Moresco[53,3], L. Moscardini[53,3,10], E. Munari[38], S. M. Niemi[50], C. Padilla[19], F. Pasian[38], K. Pedersen[57], W. J. Percival[58,59,60], V. Pettorino[61], S. Pires[37], M. Poncet[62], L. Popa[63], L. Pozzetti[3], F. Raison[1], A. Renzi[64,36], J. Rhodes[6], G. Riccio[14], E. Romelli[38], E. Rossetti[53], D. Sapone[65], B. Sartoris[66,38], P. Schneider[52], A. Secroun[39], G. Seidel[47], C. Sirignano[64,36], G. Sirri[10], L. Stanco[36], P. Tallada-Crespí[67,20], D. Tavagnacco[38], A. N. Taylor[25], I. Tereno[32,68], R. Toledo-Moreo[69], F. Torradeflot[67,20], I. Tutusaus[48], E. A. Valentijn[70], L. Valenziano[3,10], T. Vassallo[38], Y. Wang[5], A. Zacchei[38], G. Zamorani[3], J. Zoubian[39], S. Andreon[71], S. Bardelli[3], J. Graciá-Carpio[1], D. Maino[72,18,73], N. Mauri[74,10], A. Tramacere[7], E. Zucca[3], A. Alvarez Ayllon[7], H. Aussel[37], C. Baccigalupi[66,38,75,76], A. Balaguera-Antolínez[77,78], M. Ballardini[53,3,79], A. Biviano[38,66], M. Bolzonella[40], E. Bozzo[7], C. Burigana[80,81,79], R. Cabanac[82], A. Cappi[83,3], C. S. Carvalho[68], S. Casas[84], G. Castignani[53,3], A. Cooray[85], J. Coupon[7], H. M. Courtois[86], S. Davini[87], G. Desprez[7], H. Dole[34], J. A. Escartin[1], S. Escoffier[39], M. Farina[88], S. Fotopoulou[89], K. Ganga[90], J. Garcia-Bellido[91,92], K. George[2], F. Giacomini[10], G. Gozaliasl[93], H. Hildebrandt[94], I. Hook[95], O. Ilbert[96,6,5], V. Kansal[37], A. Kashlinsky[97], E. Keihanen[93], C. C. Kirkpatrick[49], A. Loureiro[98,25,99], J. Macías-Pérez[100], M. Magliocchetti[88], G. Mainetti[101], R. Maoli[102,21], M. Martinelli[21], N. Martinet[96], R. B. Metcalf[53,3], G. Morgante[3], S. Nadathur[8], A. A. Nucita[103,104,105], L. Patrizii[10], V. Popa[63], C. Porciani[52], D. Potter[106], A. Pourtsidou[107,25], P. Reimberg[82], A. G. Sánchez[1], Z. Sakr[108,109], M. Schirmer[47], E. Sefusatti[38,66,75], M. Sereno[3,10], J. Stadel[106], R. Teyssier[110], C. Valieri[10], J. Valiviita[111,112], A. Veropalumbo[113,13], and M. Viel[66,38,75,76]

(Affiliations can be found after the references)

Received 22 March 2022 / Accepted 1 June 2022

ABSTRACT

The Complete Calibration of the Color–Redshift Relation survey (C3R2) is a spectroscopic program designed to empirically calibrate the galaxy color–redshift relation to the *Euclid* depth (I_E = 24.5), a key ingredient for the success of Stage IV dark energy projects based on weak lensing cosmology. A spectroscopic calibration sample that is as representative as possible of the galaxies in the *Euclid* weak lensing sample is being collected, selecting galaxies from a self-organizing map (SOM) representation of the galaxy color space. Here, we present the results of a near-infrared *H*- and *K*-band spectroscopic campaign carried out using the LUCI instruments at the LBT. For a total of 251 galaxies, we present new highly reliable redshifts in the $1.3 \leq z \leq 1.7$ and $2 \leq z \leq 2.7$ ranges. The newly-determined redshifts populate 49 SOM cells that previously contained no spectroscopic measurements and almost twice the occupation numbers of an additional 153 SOM cells. A final optical ground-based observational effort is needed to calibrate the missing cells, in particular in the redshift range $1.7 \leq z \leq 2.7$, which lack spectroscopic calibration. In the end, *Euclid* itself will deliver telluric-free near-IR spectra that can complete the calibration.

Key words. galaxies: distances and redshifts – catalogs – surveys

⋆ The LBT is an international collaboration among institutions in the United States, Italy, and Germany. The LBT Corporation partners are: LBT Beteiligungsgesellschaft, Germany, representing the Max-Planck Society, the Astrophysical Institute Potsdam, and Heidelberg University; The University of Arizona on behalf of the Arizona university system; Istituto Nazionale di Astrofisica, Italy; The Ohio State University, and The Research Corporation, on behalf of The University of Notre Dame, University of Minnesota, and University of Virginia.

1. Introduction

The *Euclid* satellite (Laureijs et al. 2011) is scheduled for launch in 2023; it will observe galaxies to $z > 2$ over 15 000 deg^2 using two instruments: VIS, an optical imager that will reach an AB magnitude depth of 24.5 (for extended sources at $10-\sigma$, see also Euclid Collaboration 2022) with a single broad I_E filter, and NISP, a combined near-infrared imager (in Y_E, J_E, and H_E, see Euclid Collaboration 2022) and slitless spectrograph. The optical imager will determine galaxy shape distortions with unprecedented accuracy. When combined with a precise determination of the true ensemble redshift distribution, this allows the weak lensing effects caused by the distribution of matter along the line of sight to be measured and the cosmological parameters to be constrained (Euclid Collaboration 2020a).

The estimated number of weak lensing source galaxies that will be imaged from *Euclid* makes their systematic spectroscopic follow-up unfeasible; this mission is thus critically dependent upon the determination of accurate photometric redshifts ($z_{\rm phot}$). Currently, the precision of photometric redshifts based on multi-band optical surveys is to the order of $\sigma_z/(1+z) = 0.03-0.06$, and the fraction of catastrophic outliers, which are defined as objects whose $z_{\rm phot}$ differs from their spectroscopic redshift ($z_{\rm spec}$) by more than $0.15(1+z)$, is of the order of a few tens of percent (Ma et al. 2006; Hildebrandt et al. 2010). We expect that the combination of ground-based optical and *Euclid* near-infrared photometry will deliver the slightly improved requirements of the mission: $\sigma_z/(1+z) \leq 0.05$, and a fraction of catastrophic outliers less than 10% (see Laureijs et al. 2011; Euclid Collaboration 2020b).

While small changes in $z_{\rm phot}$ precision per source have a relatively small impact on cosmological parameter estimates, small systematic errors in $z_{\rm phot}$ can dominate all other uncertainties for these experiments. The aim of the C3R2 project (Masters et al. 2015, 2017, 2019; Euclid Collaboration 2020c, 2021) is to calibrate photometric redshifts by measuring accurate spectroscopic redshifts of selected objects sampling a self-organizing map (SOM), a representation of the galaxy color space. The SOM projects the high-dimensional galaxy color space onto a 2D plane. Each galaxy is assigned to a cell in this plane with given coordinates (X, Y). If this plane is sampled with enough cells, the distribution of photometric redshifts of all galaxies belonging to a cell is narrow and there is a well-defined correspondence between the position occupied by a galaxy in the multi-color space and its redshift. We can define $z_{\rm phot,SOM}$ as the average of the photometric redshifts of all galaxies belonging to the cell. By measuring spectroscopic redshifts of galaxies in each cell it is possible to calibrate the mean of the photometric redshift distribution in an efficient and homogeneous way across the galaxy color space. Regions in color space particularly difficult to calibrate because of broad or bimodal photometric redshift distributions can be identified by comparing the measured spectroscopic redshifts with $z_{\rm phot,SOM}$ and looking for deviations larger than $0.15(1+z)$. The minimum calibration requirement is to populate each SOM cell with at least one spectroscopic redshift; problematic cells might require (much) more than this. Ultimately, galaxies belonging to uncalibrated cells may be dropped from the *Euclid* weak lensing sample; for a detailed discussion see Masters et al. (2015).

In this work we continue this effort by presenting the redshift measurements of $z > 1$ galaxies collected at the Large Binocular Telescope (LBT) in the COSMOS (Capak et al. 2007; Scoville et al. 2007; Lilly et al. 2007) and VVDS (McCracken et al. 2003; Le Fèvre et al. 2004; Jarvis et al. 2013) fields, using the near-infrared LUCI spectrographs. Further data releases of optical spectra acquired at the VLT and the GRANTECAN telescopes are in preparation. The *Euclid* science working groups are actively discussing how the final ground-based dataset will be merged with the spectroscopy information delivered by the *Euclid* mission itself to perform the optimal calibration of the photometric redshifts.

The paper is organized as follows: in Sect. 2 we describe the strategy, target selection, and mask preparation; in Sect. 3 we describe the observations and data reduction; in Sect. 4 we discuss the redshift determination and the attribution of a flagging scheme consistent over the whole C3R2 survey; in Sect. 5 we present the results of the redshift assignments, and we investigate the bias of the photometric redshifts used in C3R2 and the origin of catastrophic SOM redshifts, and we discuss our success rate and SOM cell coverage; finally, we present our conclusions in Sect. 6.

2. Strategy, target selection, and mask preparation

The LBT consists of two 8 m mirrors mounted on a common structure and pointing at the same position on the sky. The LUCI1 and LUCI2 near-infrared spectrographs (Seifert et al. 2003) are mounted at the front Bent Gregorian f/15 focal stations of the LBT, and can be used in combination with masks (Buschkamp et al. 2010), designed and cut well in advance of the observations, that allow the simultaneous collection of multiple spectra. The field must be observed with identical pointings and rotation angles, but potentially with different masks and instrumental setups on the two sides. The masks cover a 4×4 arcmin^2 field of view, but only for slits placed in a 2.8 arcmin wide central stripe are optimally focused spectra delivered. Moreover, the wavelength range covered depends on the distance of a slit from the middle of a mask. At least three stars are needed to align the masks. Dedicated holes (typically 4×4 arcsec^2 big) were required until the June 2020 runs. Starting from the July 2020 run, after a change in requirements from the observatory, only one hole was necessary.

2.1. Strategy

Given the characteristics of the LBT and of the LUCI spectrographs described above, and following the strategy adopted by Euclid Collaboration (2020c, hereafter G2020), we collected spectra in the H and K bands. In the H band we can measure spectroscopic redshifts of galaxies between 1.3 and 1.7 by detecting their Hα, [N II], and [S II] emission lines, or of galaxies with redshifts between 2 and 2.7 by detecting their Hβ and [O III] lines. In the K band we can measure spectroscopic redshifts of galaxies between 2 and 2.7 by detecting their Hα, [N II], and [S II] emission lines, or (in principle) of galaxies with photometric redshifts less than 1.7 by detecting their Paschen (hereafter Pa) lines. We used the N1.8 camera, which delivers 0.25×0.25 arcsec^2 per pixels, and the G210 gratings, for which 1 arcsec-wide slits give a resolution of $R = 2950$ in the H band and $R = 2500$ in the K band. The nominal wavelength range for a centered slit is 0.202 µm and 0.328 µm in the H and K band, respectively. The central wavelength can be adjusted in the range 1.55–1.75 µm for the H band, and 2.06–2.40 µm for the K band. We optimized the central wavelength for each mask separately, based on the photometric redshifts of the observed galaxies, to maximize the likely return.

The typical angular size of the galaxies in the C3R2 catalogues is 1–2 arcsec in diameter. In order to achieve maximum

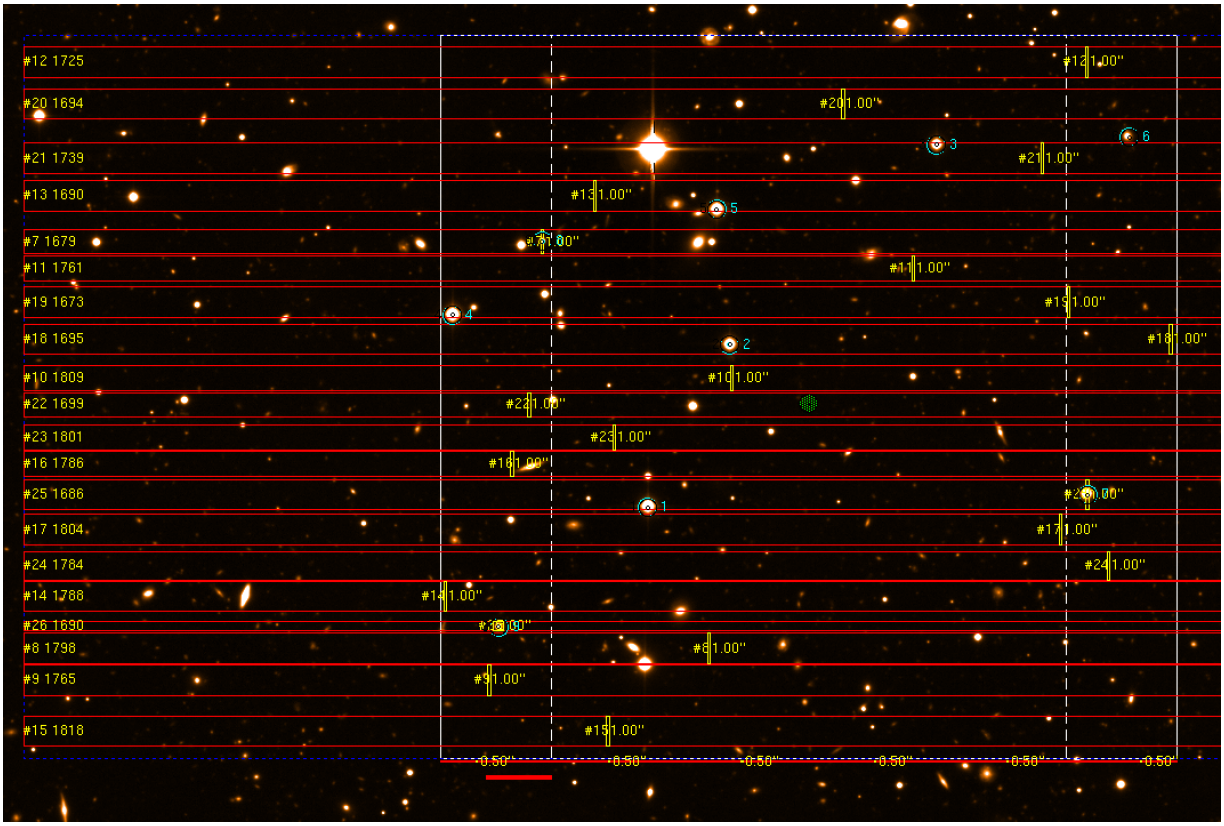

Fig. 1. COSMOS_M25H mask designed with the `lms` tool. The white square shows the LUCI field of view (4×4 arcmin^2), the long-dashed vertical lines bracket the optimal field of view for spectroscopy (2.8 arcmin wide). The green circle at the center of the field allows the mask to be moved. The cyan circles identify the alignment stars. The yellow rectangles show the slits; slit number 25 is positioned on an acquisition star to monitor seeing and transparency during the observations. The square slit number 26, also positioned on an acquisition star, allows verification of the centering of the mask after alignment. At the lower end of the mask, a series of six small holes is present for engineering purposes. Below these, the red rectangle is the area occupied by the identification number cut into the mask.

efficiency avoiding separate sky observations, we opted for an on-slit nodding strategy, which sets the default slit length to 10 arcsec and forces all slits to be parallel. Taking into account the minimum allowed distance between slits, and the necessity of cutting holes for acquisition stars, the maximum number of galaxies targeted per mask is ≈20. In reality, we never managed to observe more than 18 galaxies per mask. We ranked the list of positions and rotation angles according to the total number of galaxies observable simultaneously in the H and K bands. We observed the VVDS field in October and the COSMOS field in the months from December to May. We ended up with a list of 13 pairs of $(H + K)$ masks in the VVDS field, and 28 pairs of $(H + K)$ masks in the COSMOS field, for which at least a total $(H+K)$ 20 galaxies could be assigned, minimizing the number of repeated observations. As in G2020, we aimed to observe each mask for 2 hours, split into 36 exposures of 200 s each, dithering the mask along the slits by 2 arcsec following an ABBA pattern. The actual number of exposures collected for each mask varied according to observational conditions and constraints; see Table A.1.

2.2. Target selection and mask preparation

The selection of galaxies to be observed started from the catalogues produced by Masters et al. (2019) and used by G2020, excluding galaxies already observed with KMOS at the VLT. The catalogues adopt the photometric redshifts provided by Ilbert et al. (2006) and Laigle et al. (2016). We considered Priority 1 and Priority 2 galaxies (hereafter *primary* galaxies), as in G2020, and mapped the number of galaxies assignable to each mask as a function of the coordinates of the field centers and rotation angles, taking into consideration several constraints. At least one suitable guiding star had to be present in the allowed patrol field and within the appropriate magnitude range; at least three acquisition stars (preferably selected to have low proper motions) within the appropriate magnitude range should be present in the 4×4 arcmin^2 field of view; at least three 4×4 arcsec^2 holes (or just one from October 2020) were cut for this purpose. At least one 10×1 arcsec^2 slit was assigned to a star, to be able to reconstruct empirically the dithering pattern and measure the seeing and the relative transparency during the observations. The galaxies were placed such that the expected Hα line based on their photometric redshift fell into the wavelength range computed based on the distance to the central stripe of the field and the optimized central wavelength.

The actual design of the masks was performed with the `lms` tool[1]. During this phase, further tweakings of the centers, position angles, and slit assignments were necessary. Guide stars too near the border of the patrol field had to be changed, some acquisition stars or some slits had to be dropped or changed in length (down to 7 arcsec) because of additional constraints (e.g., one end of the mask has a regular pattern of small holes that must be avoided). Finally, the space available between the slits was

[1] https://sites.google.com/a/lbto.org/luci/preparing-to-observe/mask-preparation/lms-install

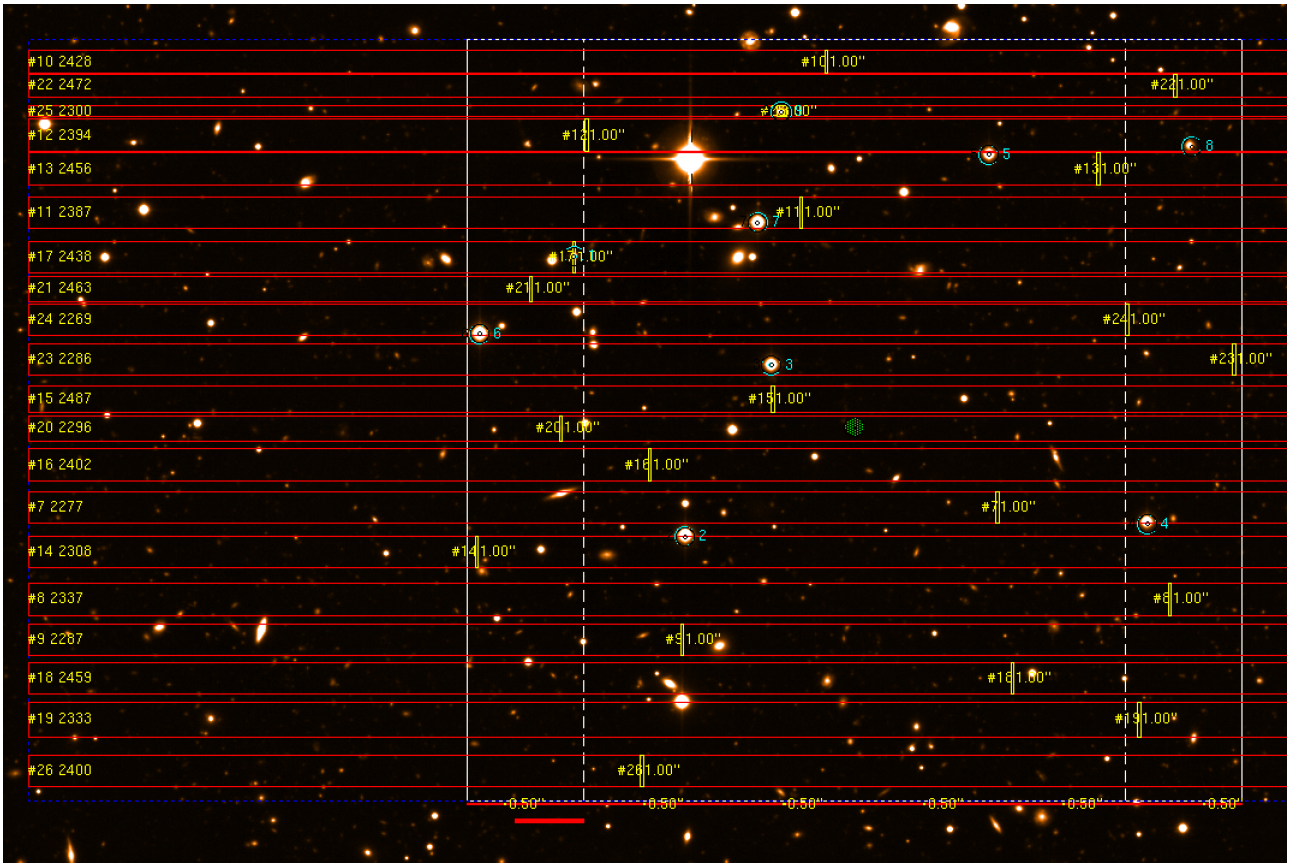

Fig. 2. COSMOS_M25K mask (see Fig. 1 for a description). Most of the slits are assigned to different objects.

filled manually with *secondary* galaxies, when possible. These are galaxies where the [O III] lines could possibly appear in the *H* band, or the Pa lines in the *K* band. Once the list of Priority 1 and 2 galaxies assigned to each mask was ready, the optimal central wavelength was calculated as the average of the Hα wavelengths, redshifted with the respective photometric redshifts. The *gbr* files detailing the masks for the cutting machine were passed to the observatory, where the masks were produced and inserted into the cryostatic dewar before each observing run.

An example of a pair of $H + K$ masks is given in the Figs. 1 and 2. All the observed masks are listed in Table A.1, where the coordinates of their centers and of their rotation angles, together with the date of the observations are given. In the end (see Table A.1), on average we extracted 12.3 galaxy spectra per mask, of which on average 9.6 were *primary*.

3. Observations and data reduction

The scripts controlling the telescope and LUCI operations were prepared using the LBTO OT software[2]. Except when one of the two LUCI spectrographs was not available, the paired approach was adopted, allowing simultaneous observation of the same field in the *H* and *K* bands. Monocular scripts were prepared for the October 2019 run (when only LUCI1 was available) and for the January 2020 run (when LUCI1 became unavailable during the run). Monocular scripts were also prepared for the observations of telluric standards. Calibration scripts to obtain dark, flat, and arc observations were also prepared in paired mode and performed during the day or at night during periods of bad weather. The observations started in visitor mode (October 2019), and continued in remote observing mode as the COVID19 emergency made international traveling impossible. Staff members from the LBT Observatory operated the instrument from Tucson for all observing runs, with scientists from the Max Planck Institute for extraterrestrial physics (M. Fabricius, S. de Nicola, R. Saglia, J. Snigula) and the Landessternwarte (J. Heidt) mainly supervising, but also directly controlling the procedures from Germany. Overall, the VVDS field was observed under good meteorological conditions; in contrast, several nights during which the COSMOS field was observed (in particular the March 2021 run), suffered from cirrus, high winds, and poor seeing.

The observation of a field follows four steps. First, an image is taken without the mask at each telescope, the acquisition stars are identified, and their positions are measured. Second, the best-fitting field rotations and translations are determined separately for the two images and applied, possibly culling the most deviant acquisition stars. Third, a second pair of images is taken through the mask to verify that acquisition and seeing-monitoring stars appear in the appropriate holes and slits. If necessary, a second translation is determined and applied to optimize the centering orthogonal to the slits. The achieved RMS precision of the alignment was typically between 0.1 and 0.3 arcsec. Fourth, the spectroscopic observations start.

After the observation of a field, or before the observation of the next one, a telluric standard was observed separately for the *H* and *K* band, putting the standard star sequentially in three slits of each mask, selected to cover the whole probed wavelength range. We observed a total of 88 masks (58 in the COSMOS field

[2] https://sites.google.com/a/lbto.org/observing-tool-manual/observing-tool/ot-installation

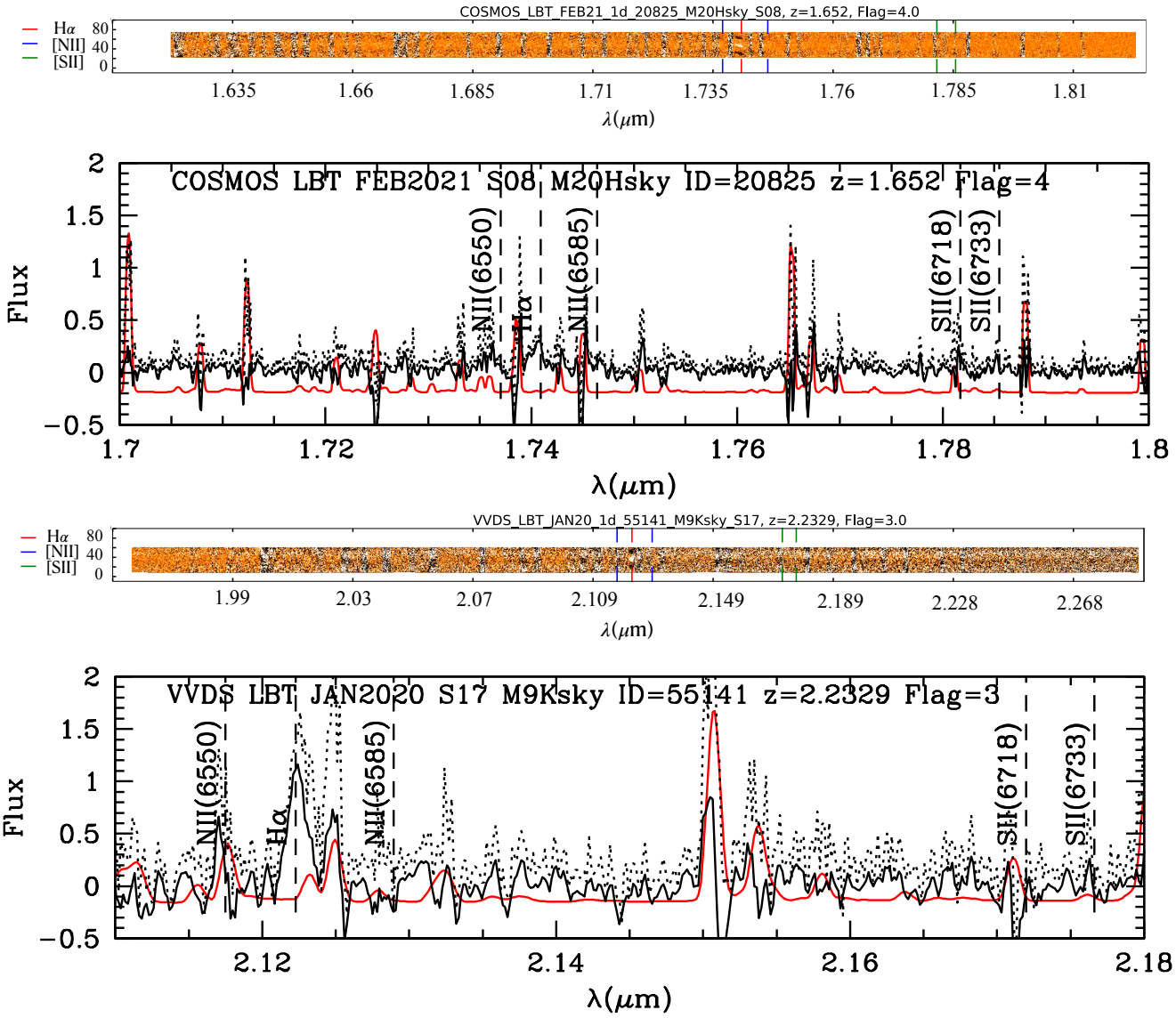

Fig. 3. One- and two-dimensional spectra with Flag = 4, 3.5, 3 of objects with $z_{\rm meas} < 2$. The 2D spectra are 10 arcsec in width, with the vertical scale given in pixels, and show the whole wavelength range (in μm) observed. The 1D spectra show the wavelength range around the relevant emission lines; the black solid lines show the measured flux (in arbitrary units with a 3 pixel smoothing), the dotted lines the flux without smoothing plus its errors, the red lines the sky (scaled down by a factor of 1000 and shifted by −0.2 flux units). The vertical dashed lines indicate the emission lines (with vacuum rest-frame wavelengths in Å) used (when visible) to measure the spectroscopic redshift (not yet corrected to the heliocentric system).

and 30 in the VVDS field), 47 in the *H* band (30 in the COSMOS field and 17 in the VVDS field), and 41 in the *K* band (28 in the COSMOS field and 13 in the VVDS field). As mentioned above, during the October 2019 run, LUCI2 was unavailable, and during the January 2020 run LUCI1 stopped working.

The data reduction was performed using the `IDL Flame` pipeline developed by Belli et al. (2018). We used the configuration which relies on the science data for tracing, extraction, and wavelength calibration, exploiting the brightness of the sky background. The steps follow the sequence described in Belli et al. (2018). First, the position of the reference star on each frame is searched for and, if detected, the flux, vertical position, and full width at half maximum (FWHM) are measured. This allows the determination of the nodding and dithering offsets of each A and B frame in the ABBA sequences. However, for many of the *K*-band pointings, the reference star cannot be detected in single frames and appears visible only after the coaddition is performed. In these cases, the list of the nominal shifts is used. After application of the bad pixel and master pixel maps, a master slit flat is computed and used to identify the slit positions and map their edges. Cutouts of the slits are produced and, after a rough wavelength calibration, individual OH emission lines are identified and fitted with a Gaussian. The relation between pixel position and wavelength is determined as a second-order polynomial for each slit row. The spatial illumination correction is determined from the detected OH lines and applied. A model of the sky is constructed following Kelson (2003) and subtracted. Finally, each sky-subtracted slit frame is rectified and wavelength calibrated before all the A and B frames are stacked together and the A-B and B-A results are produced. Their combination gives the final 2D spectra shown in Figs. 3 and 4. One-dimensional spectra are extracted after having

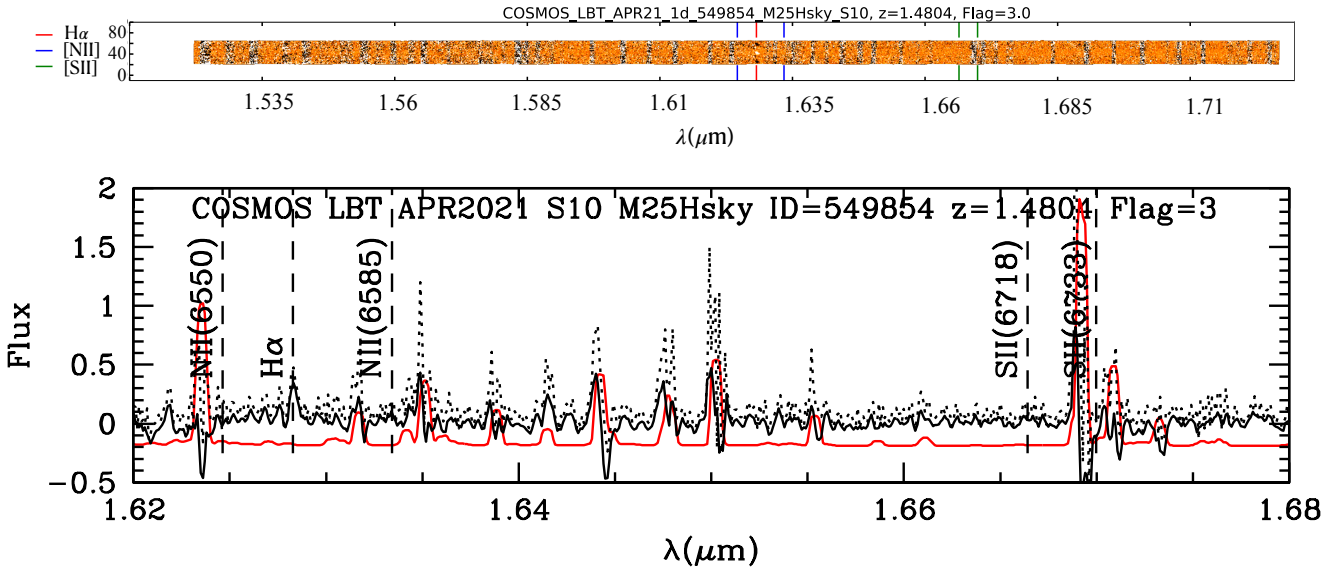

Fig. 3. continued.

identified the appropriate spatial window, either determining the spatial extent of the emission lines or of the continuum. Examples are shown in Figs. 3 and 4. We note that wavelengths refer to the vacuum and do not take into account the barycentric correction, which is applied a posteriori to the measured redshift.

4. Redshift determination and flagging

Redshifts are measured on the 1D spectra after having spotted by eye the signatures of emission lines on the 2D spectra: the presence of a sequence of a negative (black), a positive (white), and a negative (black) blob (see Figs. 3 and 4). Based on the alignment of the predicted positions of Hα, [N II], [S II], Hβ, [O III], or Pa lines with the peaks of the observed emission lines, an estimate of the redshift of the galaxy is derived, together with the appropriate flag. Following the scheme used in G2020, a Flag = 4 is assigned to redshifts with multiple good S/N line detections; a Flag = 3.5 is given to very good S/N single line detections; a Flag = 3 is given to convincing single line detections. Lower Flag (1 and 2) spectra indicate redshifts that are not secure enough for our purposes; Flag = −99 are non-detections or failed reductions. Examples of Flag = 4, 3.5, 3 spectra and redshifts are given in Figs. 3 and 4.

In a number of slits, more than one object was detected, either as a spatially separate object or on the same line of sight, but with different redshifts. In these cases multiple 1D spectra were extracted and analyzed. The correct identification was attempted by inspection of the relevant images.

The procedure described above was performed independently by two of us (RPS and RZ); discrepant assessments were discussed and resolved. We extracted 1119 spectra, of which 19 were not matched with an object from the photometric parent catalogues. We matched 292 good spectra (Flag ≥ 3): 163 in the COSMOS field, 129 in the VVDS field. The complete statistics are given in Table 1, where we list the numbers referring to *primary* spectra (targeting the Hα line) and *secondary* spectra (targeting the [O III] or Pa lines).

Table A.1 (column "Success Rate") gives the number of extracted identified spectra (a total of 1100) in each pointing together with the number of good spectra (Flag ≥ 3) and the number of primary spectra collected. The mean success rate (defined as the ratio of the number of identified good spectra over the total number of collected identified spectra) is 0.27 (0.22 in the COSMOS field and 0.37 in the VVDS field; the lower success rate in the COSMOS field stems from the suboptimal meteorological conditions under which several COSMOS masks were observed). It is higher in the *H* band (0.32; 0.28 in the COSMOS field and 0.40 in the VVDS field) than in the *K* band (0.19; 0.13 in the COSMOS field and 0.33 in the VVDS field). The success rates achieved by G2020 are better, which stems from the larger field of view (which allowed an optimized choice of good candidates), the fixed wavelength range, and the IFU available with the KMOS instrument. We investigate the properties of the galaxies with unreliable spectra (Flag < 3) in Sect. 5.

The barycentric corrections $z_{\rm helcorr} = v_{\rm helcorr}/c$ appropriate to each mask are listed in Table A.1 together with the Julian date (JD) adopted for the computation. This corresponds to the middle of the sequence of exposures. When two series of exposures observed in different nights are summed together, the JD refers to the first of the two. The barycentric corrections are computed through the `python` routine `pyals.helcorr` from `PyAstronomy`; we quote the two digits that affect the last quoted digit of the redshifts. Using the relation $1+z_{\rm spec} = (1+z_{\rm meas})\,(1+z_{\rm helcorr})$, where $z_{\rm meas}$ are the measured redshifts shown in Figs. 3 and 4, we compute the redshifts $z_{\rm spec}$ given in Table B.1 using the formula $z_{\rm spec} = z_{\rm meas} + (1+z_{\rm meas})\,z_{\rm helcorr}$. In addition, Table B.1 reports the object ID, its coordinates, the Flag, the line or ensemble of lines used (Hα plus possibly [N II] and/or [S II], [O III] plus possibly Hβ, Pa) and the name of the spectrum.

A number of objects were observed multiple times, enabling an empirical determination of the errors on our redshifts and to compare redshifts derived from the *K*- and *H*-band spectra. Figure 5 shows that the RMS uncertainty on the redshifts of objects at $z < 1.8$ with repeat observations is 0.0002, and two times larger for objects with $z > 1.8$. One COSMOS object (ID = 481647) was observed by the previous C3R2 releases, providing $z_{\rm spec} = 1.501$, identical to $z_{\rm spec} = 1.501$ obtained here. A further COSMOS object (ID = 480046) was observed by Euclid Collaboration (2021), who reported $z_{\rm spec} = 2.2705$, while our measurement is $z_{\rm spec} = 2.2702$, in line with the results discussed above. Following these findings, we quote the measured

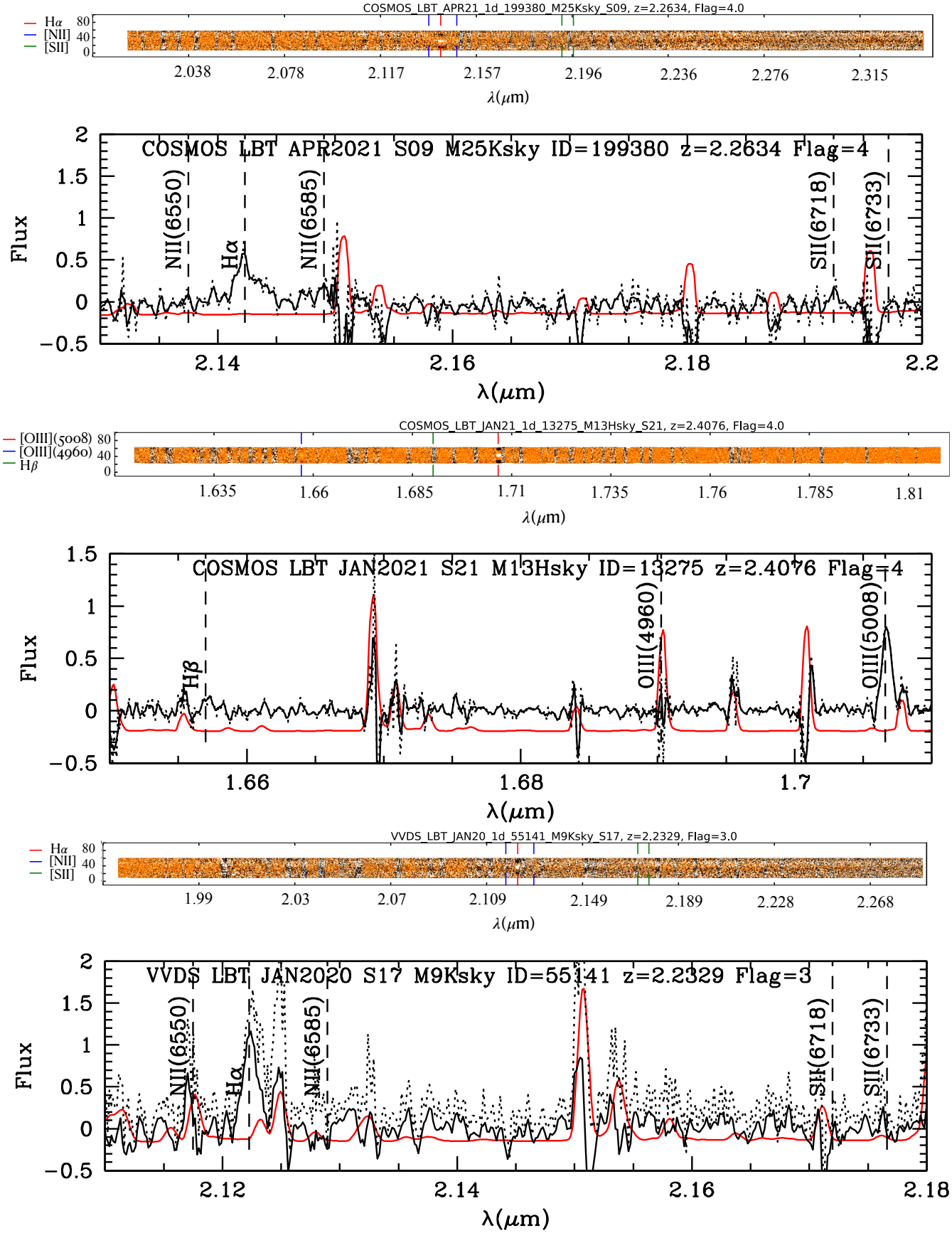

Fig. 4. One- and two-dimensional spectra with Flag = 4 and 3 of objects with $z_{meas} > 2$. Lines as in Fig. 3.

Table 1. Statistics of observed spectra.

Spectra	All	*H* band	*K* band	COSMOS	*H* band	*K* band	VVDS	*H* band	*K* band
Extracted	1119	635	484	766	424	342	353	211	142
Good	305	212	93	174	127	47	131	85	46
Identified	1100	618	482	751	410	341	349	208	141
Good	292	200	92	163	117	46	129	83	46
Primary	851	446	405	597	316	281	254	130	124
Good	249	158	91	139	94	45	110	64	46
Secondary	249	172	77	154	94	60	95	78	17
Good	43	42	1	24	23	1	19	19	0
Unidentified	19	17	2	16	15	1	4	3	1
Good	13	12	1	11	10	1	2	2	0
Primary	14	12	2	11	10	1	3	2	1
Good	8	7	1	7	6	1	1	1	0
Secondary	5	5	0	4	4	0	1	1	0
Good	5	5	0	4	4	0	1	1	0

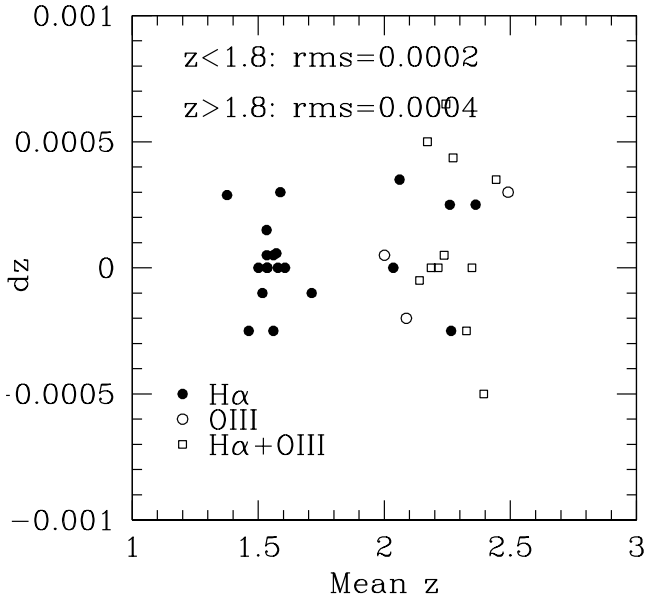

Fig. 5. Errors from repeated observations. The filled circles show the differences dz between the spectroscopic redshifts determined from two or more spectra of the same objects using the Hα line. If more than two spectra were collected, the difference to the average of the measurements is shown. The open circles show differences between redshifts based on the [O III] lines; the open squares show differences between redshifts measured using the Hα and the [O III] lines.

redshifts to four decimal digits. The redshifts determined from Hα and [O III] lines agree within the errors, with no appreciable bias.

A unique redshift $\langle z \rangle$ and flag were assigned to each object with repeated observations by averaging the available measurements; the resulting values are reported in Table 2 and used in the following figures.

Table 2. Mean redshift and flag for objects with multiple spectra.

Field	OBJ_ID	$\langle z \rangle$	$\lvert\Delta z\rvert/2$ or RMS	N	⟨Flag⟩	Lines
COSMOS	32961	1.4623	0.0003	2	3.75	Hα
COSMOS	38150	2.3945	0.0005	2	3.5	Hα+[O III]
COSMOS	402635	2.1708	0.0005	2	3.5	Hα+[O III]
COSMOS	462025	2.0875	0.0002	2	3	[O III]
COSMOS	463893	2.3473	0	2	3.5	Hα+[O III]
COSMOS	472716	1.7119	0.0001	2	3.25	Hα
COSMOS	479007	2.2725	0.0004	3	4	Hα+[O III]
COSMOS	481315	2.4910	0.0003	2	4	[O III]
COSMOS	481647	1.5010	0	2	4	Hα
COSMOS	484310	1.5879	0.0003	2	3.25	Hα
COSMOS	811438	2.3620	0.0003	2	3	Hα
VVDS	3324	1.5340	0.0001	2	4	Hα
VVDS	7941	1.5346	0	2	3.25	Hα
VVDS	22805	1.5333	0.0001	2	3.25	Hα
VVDS	24882	1.3763	0.0003	3	3.333	Hα
VVDS	24903	1.5781	0	2	3	Hα
VVDS	36412	1.5366	0	2	4	Hα
VVDS	37921	2.0007	0.0001	2	3.5	[O III]
VVDS	140031	2.2141	0	2	3.5	Hα+[O III]
VVDS	142226	1.5165	0 .0001	2	3.5	Hα
VVDS	144923	1.5600	0.0001	2	3.5	Hα
VVDS	160224	1.6061	0	3	3.667	Hα
VVDS	162982	2.2442	0.0007	2	4.0	Hα+[O III]
VVDS	163515	1.5716	0.0001	3	3.5	Hα
VVDS	165659	2.1396	0.0001	2	3.5	Hα+[O III]
VVDS	165940	2.2649	0.0002	2	3.5	Hα
VVDS	167263	2.2599	0.0002	2	3.5	Hα
VVDS	167264	2.2591	0.001	2	3	[O III]
VVDS	168107	1.5599	0.0003	2	3	Hα
VVDS	168869	2.4433	0.0004	2	3.5	Hα+[O III]
VVDS	171656	2.2376	0.0001	2	3	Hα+[O III]
VVDS	179905	2.0605	0.0003	2	4	Hα
VVDS	179990	2.0356	0	2	3	Hα
VVDS	383107	2.1861	0	2	3	Hα+[O III]
VVDS	515718	2.3259	0.0003	2	3	Hα+[O III]

5. Results

We measured good (Flag $\geq$ 3) spectroscopic redshifts for 253 objects (two of which already known): 71 with Flag = 4, 62 with Flag = 3.5, and 120 with Flag = 3. Figure 6 compares these to the photometric (left) and the SOM-based (right) redshifts. The photometric redshifts are from Ilbert et al. (2006) and Laigle et al. (2016); the SOM-based redshifts are the averages of the photometric redshifts of the galaxies belonging to the SOM cell. There are no catastrophic failures with $|z_{\rm phot} - z_{\rm spec}|/(1 + z_{\rm spec}) \geq 0.15$ and Flag $\geq$ 3. Seven objects have $|z_{\rm phot,SOM} -$

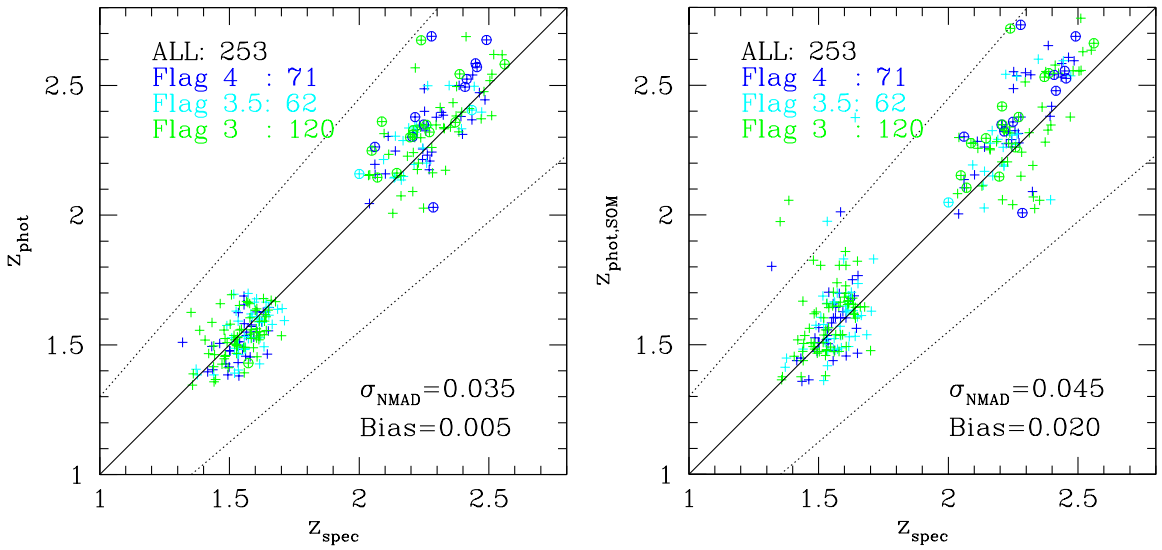

Fig. 6. Comparison between photometric and spectroscopic redshifts. *Left*: comparison between $z_{\rm phot}$ and $z_{\rm spec}$ for high-quality (Flag ≥ 3) redshift galaxies observed during the LBT campaign. Crosses show spectroscopic redshifts determined from the Hα line, circles with crosses from the [O III] lines. The dotted lines define the region outside which the $z_{\rm phot}$ is considered a catastrophic failure, defined by a redshift error $|z_{\rm phot} - z_{\rm spec}|/(1 + z_{\rm spec}) \geq 0.15$. *Right*: same as the left panel, but comparing $z_{\rm phot,SOM}$ and $z_{\rm spec}$. The values of $\sigma_{\rm NMAD} = 1.48{\rm Median}(|z - z_{\rm spec}|/(1 + z_{\rm spec}))$ and Bias = Mean$((z - z_{\rm spec})/(1 + z_{\rm spec}))$ are also given, with $z = z_{\rm phot}$ in the left plot and $z = z_{\rm phot,SOM}$ in the right.

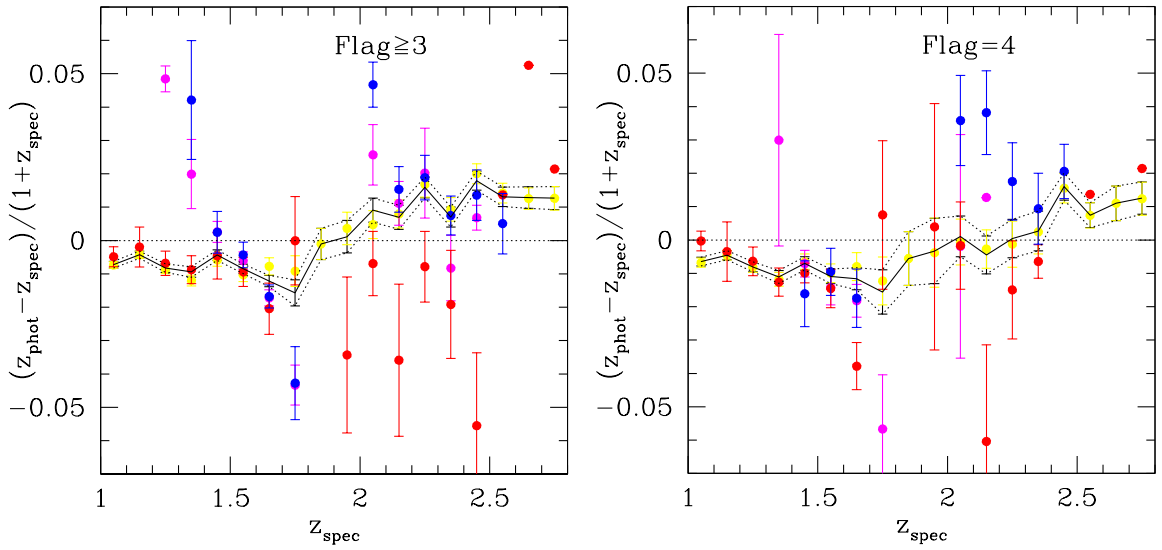

Fig. 7. Mean differences between photometric and spectroscopic redshifts. *Left*: mean differences of $(z_{\rm phot} - z_{\rm spec})/(1 + z_{\rm spec})$ of non-catastrophic failures in bins of $z_{\rm spec}$ as a function of $z_{\rm spec}$ for Flag ≥ 3 redshifts released by the C3R2 project: yellow from Masters et al. (2015, 2017, 2019); magenta from G2020; red from Euclid Collaboration (2021); blue, this paper. The black line shows the average in bins of the whole sample, the dotted lines the error range. *Right*: same, but for Flag = 4 redshifts.

$z_{\rm spec}|/(1 + z_{\rm spec}) \geq 0.15$; we examine the cells they belong to below. The values of $\sigma_{\rm NMAD} = 1.48{\rm Median}(|z - z_{\rm spec}|/(1 + z_{\rm spec}))$ and Bias = Mean$((z - z_{\rm spec})/(1 + z_{\rm spec}))$ are comparable to what achieved in previous C3R2 releases; for example G2020 quote $\sigma_{\rm NMAD} = 0.03$ and Bias $= -0.003$ when considering $z = z_{\rm phot}$ and $\sigma_{\rm NMAD} = 0.044$ and Bias $= 0.027$ when considering $z = z_{\rm phot,SOM}$.

Figure 6 shows that the agreement between photometric and spectroscopic redshifts for objects with $z_{\rm spec} < 2$ is excellent, with a mean difference of -0.006 and RMS $= 0.03$. At higher redshift, however, photometric redshifts appear systematically larger, with $\langle(z_{\rm phot} - z_{\rm spec})/(1 + z_{\rm spec})\rangle = 0.02$ and similar RMS. We investigate this issue by examining the whole C3R2 dataset published to date (see Fig. 7). When averaged in redshift bins of width 0.1, the mean difference $\langle(z_{\rm phot} - z_{\rm spec})/(1 + z_{\rm spec})\rangle$ appears slightly negative ($\approx -0.01 \pm 0.0015$) up to redshifts 1.7, and slightly positive ($\approx +0.01 \pm 0.003$) at higher redshifts, consistently in all datasets and for both Flag ≥ 3 or Flag $= 4$ redshifts. Moreover, in each bin up to redshift 1.7 the mean difference, or bias, is well determined with a signal-to-noise ratio S/N between 3 and 8. This S/N is lower (between 2 and 6) at redshifts higher than 2; the bias is unconstrained (with S/N less than 1) in between. The S/N improvement in each bin achieved by the new redshifts released here is ≤ 0.5.

This shows that the C3R2 project is able to detect and correct the residual small biases present in the most accurate available photometric redshift samples that can be used as reference in the *Euclid* mission. Therefore the tight *Euclid* requirement that the

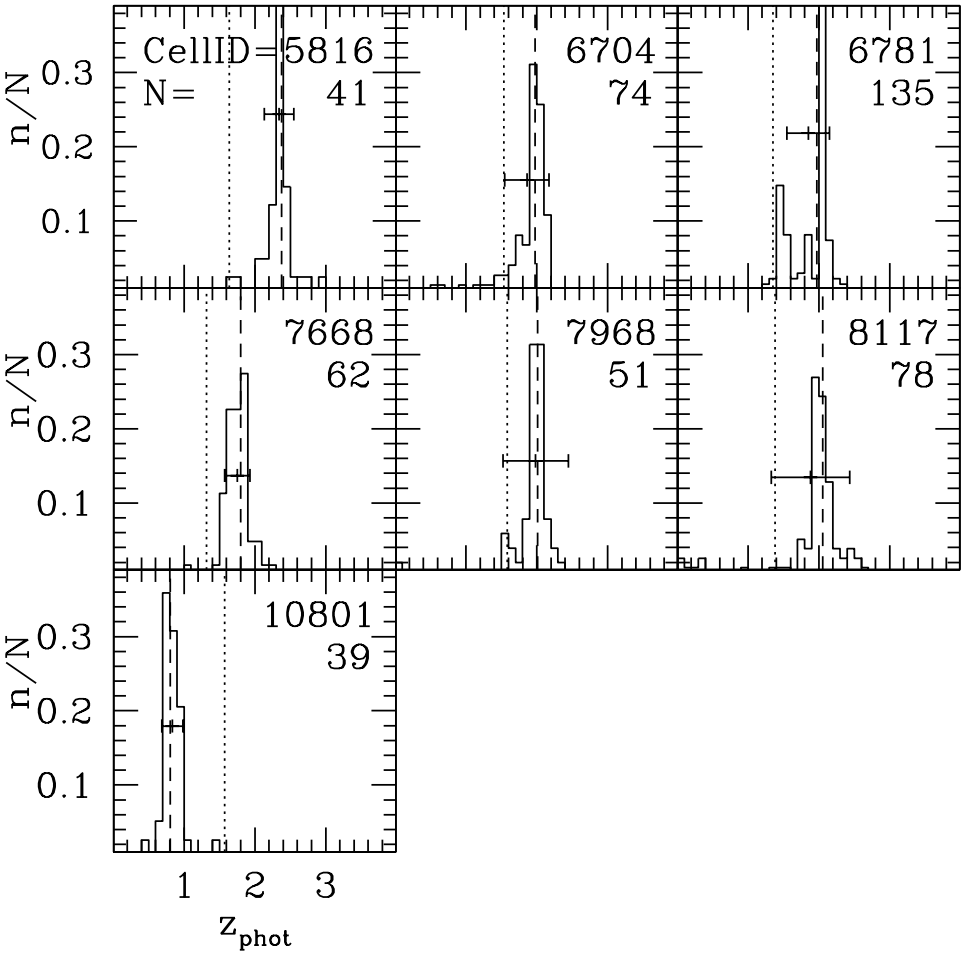

Fig. 8. Histogram of $z_{\rm phot}$ of galaxies populating each cell with $|z_{\rm phot,SOM} - z_{\rm spec}|/(1+z_{\rm spec}) > 0.15$ (right panel of Fig. 6). The distribution is normalized by dividing the number of galaxies in each $z_{\rm phot}$ bin by the total number of $z_{\rm phot}$ populating the considered cell; the number is indicated by the letter N in the top left panel, and written in the same position in the others. Similarly, the cell number (CellID) is also given in each panel. The $z_{\rm phot,SOM}$ is represented by the dashed line, whereas dotted lines indicate $z_{\rm spec}$ measured during our program. The horizontal bar centered on the mean $z_{\rm phot}$ is the RMS of the histogram.

mean redshift in each tomographic bin must be constrained at the level of $0.002(1+z)$ is achieved up to redshift 1.7 thanks to the calibration provided by the C3R2 dataset. It is almost achieved for redshifts higher than 2, but remains problematic in between, where the error on the possible residual bias is ≈0.005.

How the spectroscopic calibration of single SOM cells will be implemented when building the lensing tomographic bins for *Euclid* is still under investigation and goes beyond the scope of this paper.

Figure 6, right shows that six galaxies have $|z_{\rm phot,SOM} - z_{\rm spec}|/(1+z_{\rm spec}) > 0.15$. A seventh galaxy at $z_{\rm phot,SOM} = 0.8$ (and therefore not visible in the figure) has a similarly discrepant redshift. As noted in G2020, they belong to cells with a large spread in photometric redshifts, probing the second peak of the distribution or its tail (see Fig. 8).

Figure 9 examines the success rate as a function of redshift. As already discussed above, the success rate is lower in the *K* band and peaks when the redshifted Hα line is around the mid-redshift of either band. This is expected since the wavelength coverage depends upon the position of the galaxies on the masks, and we set the central wavelength of the spectrographs to the average of the expected Hα positions. Moreover, the focus of the spectrographs deteriorates for objects that are not within the central 2.8 arcmin stripe of the field. Similarly, the [O III] lines at $z_{\rm phot} \leq 2.1$ fall outside of the covered wavelength range in the *H* band if the objects are not in extreme positions on the masks. Overall, the success rate achieved for $z_{\rm phot} \geq 2.0$ objects targeting the Hα in the *K* band or the [O III] lines in the *H* band is similar. In contrast, we managed to detect only once (with Flag = 3) the Pa lines from the 77 targeted $z_{\rm phot} \leq 1.7$ objects in the *K* band. However, these objects were selected as fillers when space was available in the masks and no Hα targets were left. Figure 10 examines the success rate as a function of the apparent total *H*-band magnitude of the galaxies. This is not a strong function of the *H* magnitude; it is approximately 35%, down to *H* magnitudes of 23 and declining for fainter objects.

With the same motivation as in G2020, we now examine the success rate in populating SOM cells with spectra. We targeted 518 cells (388 in the COSMOS field, 194 in the VVDS field, with overlap), obtaining reliable spectra (Flag ≥ 3) for 202 (127 in COSMOS, 94 in VVDS with overlap), translating to a success rate of 39% (33% in COSMOS, 48% in VVDS). Of the 202 cells probed successfully here, 49 were empty before these observations; for the remaining 153 cells with at least one good spectroscopic redshift from previous C3R2 campaigns, on average our observations increased the number of spectroscopic redshifts per cell by 72%.

Figure 11 shows the distribution of the SOM cells probed by the current spectroscopic release, together with the cells still empty. Summing up the contributions of all C3R2 releases, we find the following. In the 839 cells with $1.3 < z_{\rm phot,SOM} < 1.7$, there are 52491 galaxies (with *I*-band magnitudes brighter than 24.5 in the COSMOS and VVDS fields). In 683 of these cells (81%), where 45370 galaxies are found (86% of the total), we collected at least one good spectroscopic redshift. In the 895 cells with $2 < z_{\rm phot,SOM} < 2.7$, there are 40013 galaxies. In 683 of these cells (74%), where 30981 galaxies are found (77% of the total), we collected at least one good spectroscopic redshift.

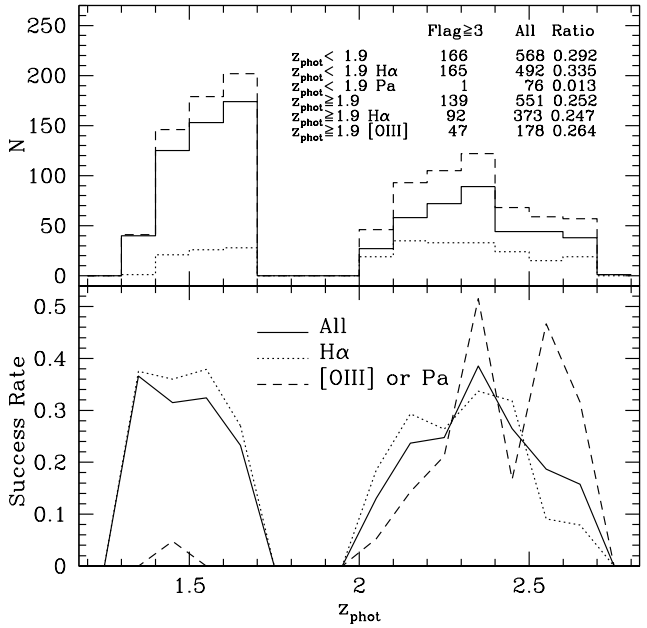

Fig. 9. Spectroscopic success rate as a function of redshift.*Top*: histogram of $z_{\rm phot}$ of targeted galaxies (dashed lines), targeting Hα (solid lines), and the [O III] or Pa lines (dotted lines). *Bottom:* success rate as a function of $z_{\rm phot}$ considering all lines (Hα, [O III], Pa, full line), based on Hα only (dotted line), or on [O III] or Pa (dashed line).

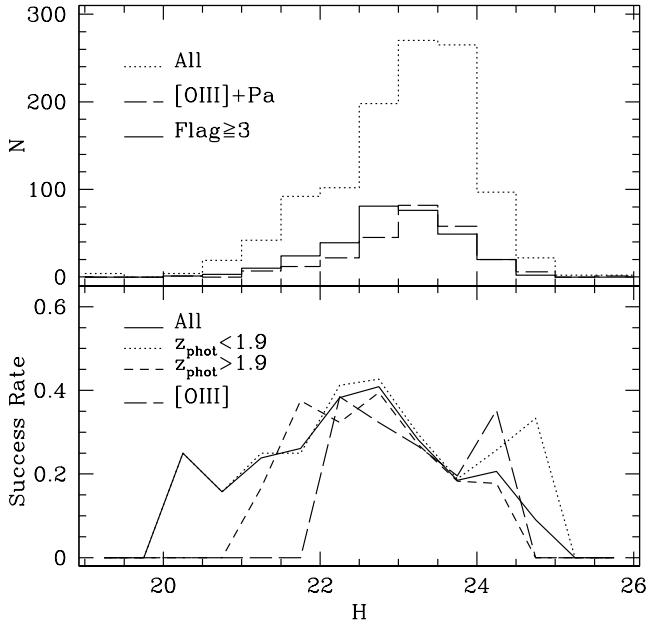

Fig. 10. Spectroscopic success rate as a function of magnitude. *Top*: histogram of the observed H total magnitudes for all observed targets (dotted line), for secondary targets (long-dashed line), and for those with high-quality spectroscopic redshifts (full line). *Bottom*: success rate as a function of H total magnitudes over the whole probed redshift range (full line), and split according to band (dotted: H band or $1.3 < z_{\rm phot} < 1.7$; dashed: K band, or $2 < z_{\rm phot} < 2.7$. The long-dashed line shows the success rate targeting the [O III] line.

6. Discussion and conclusions

We present the results of the LBT campaign to calibrate photometric redshifts in the redshift range 1.3–2.7 using the LUCI near-infrared spectrographs in the framework of the C3R2 project. We observed 88 masks, 58 in the COSMOS field and 30 in the VVDS field, with an average of 12 objects per mask, aiming to detect the Hα line for primary targets, and the [O III] or Pa lines for secondary objects. We extracted 1119 spectra, 1100 of which were identified as C3R2 galaxies. From 292 of these galaxies we were able to measure reliable spectroscopic redshifts. We assessed their precision from repeated measurements to be in the range $\Delta z \sim 0.0002$–0.0004. After averaging repeat measurements, we ended up with reliable spectroscopic redshifts for 253 galaxies, two of which with already-known values.

Comparison with the C3R2 photometric redshifts shows that none of these galaxies are catastrophic outliers. The values of $\sigma_{\rm NMAD}$ and the bias are comparable to those reported in the previous C3R2 releases. Analyzing the whole C3R2 spectroscopic database published to date, we detect a small systematic shift $\langle(z_{\rm phot} - z_{\rm spec})/(1 + z_{\rm spec})\rangle$ on the order of -0.01 ± 0.0015 in the redshift range $1.3 < z_{\rm phot} < 1.8$ and of $+0.01 \pm 0.003$ in the range $2 < z_{\rm phot} < 2.7$. This is relevant for the calibration of the redshifts of SOM cells in these redshift ranges, essentially matching the *Euclid* requirement of knowing the mean redshift of each tomografic bin to $0.002(1+z)$. Our redshift determinations populate 49 SOM cells with no prior spectroscopic measurements, approximately doubling the occupation numbers of an additional 153 cells. Seven SOM cells have $|z_{\rm phot,SOM} - z_{\rm spec}|/(1 + z_{\rm spec}) \geq 0.15$; they have a large spread in photometric redshifts, and our objects probe the second peak of the distribution or its tail.

In the redshift range 1.3–1.7 there are still 156 cells (19%) without at least one good spectroscopic redshift; in these cells that lack a spectroscopic calibration we find only 14% of the galaxy population. In the redshift range 2–2.7 there are 232 cells (26%) without at least one good spectroscopic redshift; in these cells we find 23% of the galaxy population. In between, in the redshift range 1.7 and 2 where telluric absorption makes the direct observation of Hα impossible, the number of cells without at least one good spectroscopic redshift is 126 (28%); in these cells we find 26% of the galaxy population with redshifts between 1.7 and 2. The redshift bias $\langle(z_{\rm phot} - z_{\rm spec})/(1 + z_{\rm spec})\rangle$ is not well constrained, with an error (0.005) larger than the *Euclid* requirement.

Two questions arise. First, is it worth attempting to calibrate the missing cells in the H and K bands with LUCI at the LBT? Probably not, since their density is too low for the field of view available. Moreover, G2020 found that most of them have low star formation rates, making the detection of emission lines very difficult, and the success rate (around 30%) of the present campaign is not particularly encouraging. Second, is it worth attempting the calibration of the cells missing in the redshift range 1.7–2 with ground-based facilities? Detecting the Hγ, Hβ, and [O III] lines in the J band up to redshift 2, 1.9, and 1.8, respectively, could be possible with an increasing probability of success. Whether the LBT with the LUCI spectrographs should be used for such a campaign depends on the density on the sky of the objects needing spectra. However, the difficult remaining sources at these redshifts are primarily passive galaxies, and so spectroscopic searches for Balmer and [O III] emission lines are unlikely to be efficient or successful. A costly solution could be ground-based (optical) absorption-line spectroscopy. A release of optical spectra gathered at the VLT and the GRANTECAN telescopes is in preparation. In the end the (possibly partial) natural solution will come from *Euclid* itself: its spectroscopic program will deliver near-infrared spectra in the relevant redshift range free of telluric absorption. The survey is designed to detect emission lines down to 2×10^{-16} erg s^{-1} cm^{-2}

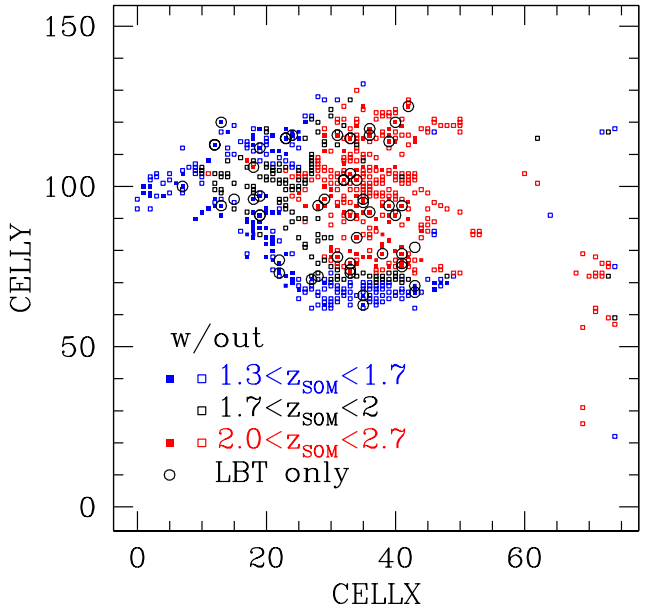

Fig. 11. Cells probed by the current spectroscopic release (filled squares) and cells still lacking spectroscopy (empty squares). Blue cells have $1.3 < z_{\rm phot,SOM} < 1.7$, black cells have $1.7 < z_{\rm phot,SOM} < 2.0$, and red cells have $2.0 < z_{\rm phot,SOM} < 2.7$. Open circles are the 49 cells without spectroscopy before this release. The circles without a centered square have $z_{\rm phot,SOM}$ outside the probed range.

at 3.5σ in the wide configuration, and reach up to 2 mag fainter levels in the deep fields (Euclid Collaboration 2022), or 3 to 6×10^{-17} erg s^{-1} cm^{-2}. Using the Hα fluxes measured by G2020, we estimate that 60–90% of the sources will be detected within these limits in the deep fields. Therefore, the mission itself will provide enough spectra to finish the photometric redshift calibration in the near-infrared range to the required precision. In particular, a question that needs to be clarified is whether in a given SOM cell the galaxies for which we are able or unable to measure a spectroscopic redshift might have different redshift distributions.

Acknowledgements. The Euclid Consortium acknowledges the European Space Agency and a number of agencies and institutes that have supported the development of *Euclid*, in particular the Academy of Finland, the Agenzia Spaziale Italiana, the Belgian Science Policy, the Canadian Euclid Consortium, the French Centre National d'Etudes Spatiales, the Deutsches Zentrum für Luft- und Raumfahrt, the Danish Space Research Institute, the Fundação para a Ciência e a Tecnologia, the Ministerio de Ciencia e Innovación, the National Aeronautics and Space Administration, the National Astronomical Observatory of Japan, the Netherlandse Onderzoekschool Voor Astronomie, the Norwegian Space Agency, the Romanian Space Agency, the State Secretariat for Education, Research and Innovation (SERI) at the Swiss Space Office (SSO), and the United Kingdom Space Agency. A complete and detailed list is available on the *Euclid* web site (http://www.euclid-ec.org). R.S., M.F., V.G., R.B. acknowledge support by the Deutsches Zentrum für Luft- und Raumfahrt (DLR) grant 50 QE 1101. The work of DS was carried out at the Jet Propulsion Laboratory, California Institute of Technology, under a contract with NASA. We thank the staff of the LBT observatory for their support during the mask preparation and the execution of the observations. H. Hildebrandt is supported by a Heisenberg grant of the Deutsche Forschungsgemeinschaft (Hi 1495/5-1) as well as an ERC Consolidator Grant (No. 770935).

References

Belli, S., Contursi, A., & Davies, R. I. 2018, MNRAS, 478, 2097
Buschkamp, P., Hofmann, R., Gemperlein, H., et al. 2010, in Ground-based and Airborne Instrumentation for Astronomy III, eds. I. S. McLean, S. K. Ramsay, & H. Takami , SPIE Conf. Ser., 7735, 773579
Capak, P., Aussel, H., Ajiki, M., et al. 2007, ApJS, 172, 99
Euclid Collaboration (Blanchard, A., et al.) 2020a, A&A, 642, A191
Euclid Collaboration (Desprez, G., et al.) 2020b, A&A, 644, A31
Euclid Collaboration (Guglielmo, V., et al.) 2020c, A&A, 642, A192
Euclid Collaboration (Stanford, S. A., et al.) 2021, ApJS, 256, 9
Euclid Collaboration (Scaramella, R., et al.) 2022, A&A, 662, A112
Hildebrandt, H., Arnouts, S., Capak, P., et al. 2010, A&A, 523, A31
Ilbert, O., Arnouts, S., McCracken, H. J., et al. 2006, A&A, 457, 841
Jarvis, M. J., Bonfield, D. G., Bruce, V. A., et al. 2013, MNRAS, 428, 1281
Kelson, D. D. 2003, PASP, 115, 688
Laigle, C., McCracken, H. J., Ilbert, O., et al. 2016, ApJS, 224, 24
Laureijs, R., Amiaux, J., Arduini, S., et al. 2011, ArXiv e-prints [arXiv:1110.3193]
Le Fèvre, O., Mellier, Y., McCracken, H. J., et al. 2004, A&A, 417, 839
Lilly, S. J., Le Fèvre, O., Renzini, A., et al. 2007, ApJS, 172, 70
Ma, Z., Hu, W., & Huterer, D. 2006, ApJ, 636, 21
Masters, D., Capak, P., Stern, D., et al. 2015, ApJ, 813, 53
Masters, D. C., Stern, D. K., Cohen, J. G., et al. 2017, ApJ, 841, 111
Masters, D. C., Stern, D. K., Cohen, J. G., et al. 2019, ApJ, 877, 81
McCracken, H. J., Radovich, M., Bertin, E., et al. 2003, A&A, 410, 17
Scoville, N., Aussel, H., Brusa, M., et al. 2007, ApJS, 172, 1
Seifert, W., Appenzeller, I., Baumeister, H., et al. 2003, in Instrument Design and Performance for Optical/Infrared Ground-based Telescopes, eds. M. Iye, & A. F. M. Moorwood , SPIE Conf. Ser., 4841, 962

[1] Max Planck Institute for Extraterrestrial Physics, Giessenbachstr. 1, 85748 Garching, Germany
e-mail: saglia@mpe.mpg.de
[2] Universitäts-Sternwarte München, Fakultät für Physik, Ludwig-Maximilians-Universität München, Scheinerstrasse 1, 81679 München, Germany
[3] INAF-Osservatorio di Astrofisica e Scienza dello Spazio di Bologna, Via Piero Gobetti 93/3, 40129 Bologna, Italy
[4] Landessternwarte, Zentrum für Astronomie der Universität Heidelberg, Königstuhl 12, 69117 Heidelberg, Germany
[5] Infrared Processing and Analysis Center, California Institute of Technology, Pasadena, CA 91125, USA
[6] Jet Propulsion Laboratory, California Institute of Technology, 4800 Oak Grove Drive, Pasadena, CA 91109, USA
[7] Department of Astronomy, University of Geneva, ch. d'Ecogia 16, 1290 Versoix, Switzerland
[8] Institute of Cosmology and Gravitation, University of Portsmouth, Portsmouth PO1 3FX, UK
[9] Dipartimento di Fisica e Astronomia, Universitá di Bologna, Via Gobetti 93/2, 40129 Bologna, Italy
[10] INFN-Sezione di Bologna, Viale Berti Pichat 6/2, 40127 Bologna, Italy
[11] INAF-Osservatorio Astrofisico di Torino, Via Osservatorio 20, 10025 Pino Torinese (TO), Italy
[12] Dipartimento di Fisica, Universitá degli studi di Genova, and INFN-Sezione di Genova, via Dodecaneso 33, 16146 Genova, Italy
[13] INFN-Sezione di Roma Tre, Via della Vasca Navale 84, 00146 Roma, Italy
[14] INAF-Osservatorio Astronomico di Capodimonte, Via Moiariello 16, 80131 Napoli, Italy
[15] Instituto de Astrofísica e Ciências do Espaço, Universidade do Porto, CAUP, Rua das Estrelas, 4150-762 Porto, Portugal
[16] Dipartimento di Fisica, Universitá degli Studi di Torino, Via P. Giuria 1, 10125 Torino, Italy
[17] INFN-Sezione di Torino, Via P. Giuria 1, 10125 Torino, Italy
[18] INAF-IASF Milano, Via Alfonso Corti 12, 20133 Milano, Italy
[19] Institut de Física d'Altes Energies (IFAE), The Barcelona Institute of Science and Technology, Campus UAB, 08193 Bellaterra (Barcelona), Spain
[20] Port d'Informació Científica, Campus UAB, C. Albareda s/n, 08193 Bellaterra (Barcelona), Spain
[21] INAF-Osservatorio Astronomico di Roma, Via Frascati 33, 00078 Monteporzio Catone, Italy
[22] INFN section of Naples, Via Cinthia 6, 80126 Napoli, Italy

[23] Department of Physics "E. Pancini", University Federico II, Via Cinthia 6, 80126 Napoli, Italy
[24] Institut national de physique nucléaire et de physique des particules, 3 rue Michel-Ange, 75794 Paris Cedex 16, France
[25] Institute for Astronomy, University of Edinburgh, Royal Observatory, Blackford Hill, Edinburgh EH9 3HJ, UK
[26] Jodrell Bank Centre for Astrophysics, Department of Physics and Astronomy, University of Manchester, Oxford Road, Manchester M13 9PL, UK
[27] ESAC/ESA, Camino Bajo del Castillo, s/n., Urb. Villafranca del Castillo, 28692 Villanueva de la Cañada, Madrid, Spain
[28] European Space Agency/ESRIN, Largo Galileo Galilei 1, 00044 Frascati, Roma, Italy
[29] Univ Lyon, Univ Claude Bernard Lyon 1, CNRS/IN2P3, IP2I Lyon, UMR 5822, 69622 Villeurbanne, France
[30] Institute of Physics, Laboratory of Astrophysics, Ecole Polytechnique Fédérale de Lausanne (EPFL), Observatoire de Sauverny, 1290 Versoix, Switzerland
[31] Mullard Space Science Laboratory, University College London, Holmbury St Mary, Dorking, Surrey RH5 6NT, UK
[32] Departamento de Física, Faculdade de Ciências, Universidade de Lisboa, Edifício C8, Campo Grande, 1749-016 Lisboa, Portugal
[33] Instituto de Astrofísica e Ciências do Espaço, Faculdade de Ciências, Universidade de Lisboa, Campo Grande, 1749-016 Lisboa, Portugal
[34] Université Paris-Saclay, CNRS, Institut d'astrophysique spatiale, 91405 Orsay, France
[35] Department of Physics, Oxford University, Keble Road, Oxford OX1 3RH, UK
[36] INFN-Padova, Via Marzolo 8, 35131 Padova, Italy
[37] AIM, CEA, CNRS, Université Paris-Saclay, Université de Paris, 91191 Gif-sur-Yvette, France
[38] INAF-Osservatorio Astronomico di Trieste, Via G. B. Tiepolo 11, 34143 Trieste, Italy
[39] Aix-Marseille Univ, CNRS/IN2P3, CPPM, Marseille, France
[40] Istituto Nazionale di Astrofisica (INAF) – Osservatorio di Astrofisica e Scienza dello Spazio (OAS), Via Gobetti 93/3, 40127 Bologna, Italy
[41] Istituto Nazionale di Fisica Nucleare, Sezione di Bologna, Via Irnerio 46, 40126 Bologna, Italy
[42] INAF-Osservatorio Astronomico di Padova, Via dell'Osservatorio 5, 35122 Padova, Italy
[43] Institute of Theoretical Astrophysics, University of Oslo, PO Box 1029 Blindern, 0315 Oslo, Norway
[44] Leiden Observatory, Leiden University, Niels Bohrweg 2, 2333 CA Leiden, The Netherlands
[45] von Hoerner & Sulger GmbH, SchloßPlatz 8, 68723 Schwetzingen, Germany
[46] Technical University of Denmark, Elektrovej 327, 2800 Kgs. Lyngby, Denmark
[47] Max-Planck-Institut für Astronomie, Königstuhl 17, 69117 Heidelberg, Germany
[48] Université de Genève, Département de Physique Théorique and Centre for Astroparticle Physics, 24 quai Ernest-Ansermet, 1211 Genève 4, Switzerland
[49] Department of Physics and Helsinki Institute of Physics, Gustaf Hällströmin katu 2, 00014 University of Helsinki, Finland
[50] European Space Agency/ESTEC, Keplerlaan 1, 2201 AZ Noordwijk, The Netherlands
[51] NOVA optical infrared instrumentation group at ASTRON, Oude Hoogeveensedijk 4, 7991 PD Dwingeloo, The Netherlands
[52] Argelander-Institut für Astronomie, Universität Bonn, Auf dem Hügel 71, 53121 Bonn, Germany
[53] Dipartimento di Fisica e Astronomia "Augusto Righi" – Alma Mater Studiorum Università di Bologna, via Piero Gobetti 93/2, 40129 Bologna, Italy
[54] Department of Physics, Institute for Computational Cosmology, Durham University, South Road, DH1 3LE, UK
[55] Institut d'Astrophysique de Paris, UMR 7095, CNRS, and Sorbonne Université, 98 bis boulevard Arago, 75014 Paris, France
[56] University of Applied Sciences and Arts of Northwestern Switzerland, School of Engineering, 5210 Windisch, Switzerland
[57] Department of Physics and Astronomy, University of Aarhus, Ny Munkegade 120, 8000 Aarhus C, Denmark
[58] Centre for Astrophysics, University of Waterloo, Waterloo, Ontario N2L 3G1, Canada
[59] Department of Physics and Astronomy, University of Waterloo, Waterloo, Ontario N2L 3G1, Canada
[60] Perimeter Institute for Theoretical Physics, Waterloo, Ontario N2L 2Y5, Canada
[61] Université Paris-Saclay, Université Paris Cité, CEA, CNRS, Astrophysique, Instrumentation et Modélisation Paris-Saclay, 91191 Gif-sur-Yvette, France
[62] Centre National d'Etudes Spatiales, Toulouse, France
[63] Institute of Space Science, Bucharest 077125, Romania
[64] Dipartimento di Fisica e Astronomia "G.Galilei", Universitá di Padova, Via Marzolo 8, 35131 Padova, Italy
[65] Departamento de Física, FCFM, Universidad de Chile, Blanco Encalada 2008, Santiago, Chile
[66] IFPU, Institute for Fundamental Physics of the Universe, via Beirut 2, 34151 Trieste, Italy
[67] Centro de Investigaciones Energéticas, Medioambientales y Tecnológicas (CIEMAT), Avenida Complutense 40, 28040 Madrid, Spain
[68] Instituto de Astrofísica e Ciências do Espaço, Faculdade de Ciências, Universidade de Lisboa, Tapada da Ajuda, 1349-018 Lisboa, Portugal
[69] Universidad Politécnica de Cartagena, Departamento de Electrónica y Tecnología de Computadoras, 30202 Cartagena, Spain
[70] Kapteyn Astronomical Institute, University of Groningen, PO Box 800, 9700 AV Groningen, The Netherlands
[71] INAF-Osservatorio Astronomico di Brera, Via Brera 28, 20122 Milano, Italy
[72] Dipartimento di Fisica "Aldo Pontremoli", Universitá degli Studi di Milano, Via Celoria 16, 20133 Milano, Italy
[73] INFN-Sezione di Milano, Via Celoria 16, 20133 Milano, Italy
[74] Dipartimento di Fisica e Astronomia "Augusto Righi" – Alma Mater Studiorum Universitá di Bologna, Viale Berti Pichat 6/2, 40127 Bologna, Italy
[75] INFN, Sezione di Trieste, Via Valerio 2, 34127 Trieste TS, Italy
[76] SISSA, International School for Advanced Studies, Via Bonomea 265, 34136 Trieste TS, Italy
[77] Instituto de Astrofísica de Canarias (IAC); Departamento de Astrofísica, Universidad de La Laguna (ULL), 38200 La Laguna, Tenerife, Spain
[78] Instituto de Astrofísica de Canarias, Calle Vía Láctea s/n, San Cristóbal de La Laguna, 38204 Tenerife, Spain
[79] INFN-Bologna, Via Irnerio 46, 40126 Bologna, Italy
[80] Dipartimento di Fisica e Scienze della Terra, Universitá degli Studi di Ferrara, Via Giuseppe Saragat 1, 44122 Ferrara, Italy
[81] INAF, Istituto di Radioastronomia, Via Piero Gobetti 101, 40129 Bologna, Italy
[82] Institut d'Astrophysique de Paris, 98bis boulevard Arago, 75014 Paris, France
[83] Université Côte d'Azur, Observatoire de la Côte d'Azur, CNRS, Laboratoire Lagrange, Bd de l'Observatoire, CS 34229, 06304 Nice Cedex 4, France
[84] Institute for Theoretical Particle Physics and Cosmology (TTK), RWTH Aachen University, 52056 Aachen, Germany
[85] Department of Physics & Astronomy, University of California Irvine, Irvine, CA 92697, USA
[86] University of Lyon, UCB Lyon 1, CNRS/IN2P3, IUF, IP2I Lyon, Villeurbanne, France
[87] INFN-Sezione di Genova, Via Dodecaneso 33, 16146 Genova, Italy
[88] INAF-Istituto di Astrofisica e Planetologia Spaziali, via del Fosso del Cavaliere, 100, 00100 Roma, Italy
[89] School of Physics, HH Wills Physics Laboratory, University of Bristol, Tyndall Avenue, Bristol BS8 1TL, UK
[90] Université Paris Cité, CNRS, Astroparticule et Cosmologie, 75013 Paris, France

[91] Departamento de Física Teórica, Facultad de Ciencias, Universidad Autónoma de Madrid, 28049 Cantoblanco, Madrid, Spain
[92] Instituto de Física Teórica UAM-CSIC, Campus de Cantoblanco, 28049 Madrid, Spain
[93] Department of Physics, PO Box 64, 00014 University of Helsinki, Finland
[94] Ruhr University Bochum, Faculty of Physics and Astronomy, Astronomical Institute (AIRUB), German Centre for Cosmological Lensing (GCCL), 44780 Bochum, Germany
[95] Department of Physics, Lancaster University, Lancaster LA1 4YB, UK
[96] Aix-Marseille Univ, CNRS, CNES, LAM, Marseille, France
[97] Code 665, NASA Goddard Space Flight Center, Greenbelt, MD 20771 and SSAI, Lanham, MD 20770, USA
[98] Astrophysics Group, Blackett Laboratory, Imperial College London, London SW7 2AZ, UK
[99] Department of Physics and Astronomy, University College London, Gower Street, London WC1E 6BT, UK
[100] Univ. Grenoble Alpes, CNRS, Grenoble INP, LPSC-IN2P3, 53, Avenue des Martyrs, 38000 Grenoble, France
[101] Centre de Calcul de l'IN2P3, 21 avenue Pierre de Coubertin, 69627 Villeurbanne Cedex, France
[102] Dipartimento di Fisica, Sapienza Università di Roma, Piazzale Aldo Moro 2, 00185 Roma, Italy
[103] Department of Mathematics and Physics E. De Giorgi, University of Salento, Via per Arnesano, CP-I93, 73100 Lecce, Italy
[104] INAF-Sezione di Lecce, c/o Dipartimento Matematica e Fisica, Via per Arnesano, 73100 Lecce, Italy
[105] INFN, Sezione di Lecce, Via per Arnesano, CP-193, 73100 Lecce, Italy
[106] Institute for Computational Science, University of Zurich, Winterthurerstrasse 190, 8057 Zurich, Switzerland
[107] Higgs Centre for Theoretical Physics, School of Physics and Astronomy, The University of Edinburgh, Edinburgh EH9 3FD, UK
[108] Université St Joseph; Faculty of Sciences, Beirut, Lebanon
[109] Institut de Recherche en Astrophysique et Planétologie (IRAP), Université de Toulouse, CNRS, UPS, CNES, 14 Av. Edouard Belin, 31400 Toulouse, France
[110] Department of Astrophysical Sciences, Peyton Hall, Princeton University, Princeton, NJ 08544, USA
[111] Department of Physics, PO Box 35 (YFL), 40014 University of Jyväskylä, Finland
[112] Helsinki Institute of Physics, Gustaf Hällströmin katu 2, University of Helsinki, Helsinki, Finland
[113] Department of Mathematics and Physics, Roma Tre University, Via della Vasca Navale 84, 00146 Rome, Italy

Appendix A: Table A.1

Table A.1. List of the observed masks.

Field	Mask ID	RA_{cen} (hms)	Dec_{cen} (dms)	Rot.Angle (deg)	nExp (×200 s)	UT Date (yyyy.mm.dd)	JD	$z_{helcorr}$ ($\times 10^5$)	Success Rate (Flag ≥ 3/Prim/Obs)
VVDS	M1H	022614.372	−045554.320	15	36	2019-10-03	2458759.83	3.6	6/12/14
VVDS	M2H	022622.493	−045356.990	20	36	2019-10-03	2458759.95	3.5	7/8/12
VVDS	M3H	022622.572	−045759.610	−16	36	2019-10-07	2458763.80	3.0	4/7/12
VVDS	M4H	022606.238	−045557.250	0	36	2019-10-07	2458764.93	2.7	4/10/14
VVDS	M5H	022630.656	−044152.010	75	36	2019-10-09	2458765.82	2.7	7/7/12
VVDS	M9H	022550.162	−045358.310	50	22	2020-01-19	2458867.75	−9.7	6/9/13
VVDS	M9K	022550.162	−045358.310	50	23	2020-01-19	2458867.75	−9.7	1/6/7
VVDS	M12K	022437.840	−041546.890	145	26	2020-01-23	2458871.61	−9.7	0/6/7
COSMOS	M1H	095839.234	+015608.340	160	36	2020-03-16	2458924.65	−3.9	6/13/16
COSMOS	M1K	095839.234	+015608.340	160	36	2020-03-16	2458924.65	−3.9	2/11/13
COSMOS	M2H	100024.224	+021252.150	−10	33	2020-03-16	2458924.85	−4.0	1/6/7
COSMOS	M2K	100024.224	+021252.150	−10	33	2020-03-16	2458924.85	−4.0	0/4/7
COSMOS	M3H	095856.377	+020807.150	135	36	2020-03-17	2458925.65	−4.0	6/12/14
COSMOS	M3K	095856.377	+020807.150	135	36	2020-03-17	2458925.65	−4.0	1/8/12
VVDS	M6H_1	022726.448	−045159.520	−105	25	2020-10-03	2459125.32	3.5	4/7/12
VVDS	M6K_1	022726.448	−045159.520	−105	25	2020-10-03	2459125.32	3.5	2/10/11
VVDS	M7H	022445.672	−040142.190	195	35	2020-10-03	2459125.46	3.6	4/3/12
VVDS	M7K	022445.672	−040142.190	195	35	2020-10-03	2459125.46	3.6	4/14/15
VVDS	M8H	022631.827	−043805.980	240	36	2020-10-04	2459126.30	3.3	4/6/11
VVDS	M8K	022631.827	−043805.980	240	36	2020-10-04	2459126.30	3.3	4/6/9
VVDS	M10H	022534.064	−040945.080	170	36	2020-10-04	2459126.45	3.4	4/11/14
VVDS	M10K	022534.064	−040945.080	170	36	2020-10-04	2459126.45	3.4	3/8/13
VVDS	M12H	022437.840	−041546.890	145	36	2020-10-05	2459127.46	3.2	5/6/12
VVDS	M12K	022437.840	−041546.890	145	36	2020-10-06	2459127.46	3.2	6/11/11
VVDS	M11H	022526.034	−043954.090	335	36	2020-10-05	2459127.59	3.3	5/7/12
VVDS	M11K	022526.034	−043954.090	335	36	2020-10-05	2459127.59	3.3	5/11/11
VVDS	M13H	022429.716	−044355.300	340	36	2020-10-06	2459128.38	3.0	5/8/11
VVDS	M13K	022429.716	−044355.300	340	37	2020-10-06	2459128.38	3.0	5/10/10
VVDS	M14H_1	022630.358	−043954.870	70	11	2020-10-06	2459128.50	3.1	5/5/9
VVDS	M14K_1	022630.358	−043954.870	70	11	2020-10-06	2459128.50	3.1	8/11/11
VVDS	M14H_2	022630.358	−043954.870	70	30	2020-10-07	2459128.50	3.1	summed to M14H_1
VVDS	M14K_2	022630.358	−043954.870	70	27	2020-10-07	2459128.50	3.1	summed to M14K_1
VVDS	M4H	022606.238	−045557.250	0	36	2020-10-07	2459129.44	3.0	4/10/14
VVDS	M4K	022606.238	−045557.250	0	36	2020-10-07	2459129.44	3.0	2/9/13
VVDS	M3H	022622.572	−045759.610	−16	36	2020-10-04	2459130.31	2.7	3/7/12
VVDS	M3K	022622.572	−045759.610	−16	36	2020-10-04	2459130.31	2.7	1/10/11
VVDS	M6H_0	022726.448	−045159.520	−105	3	2020-10-07	2459125.32	3.5	summed to M6H_1
VVDS	M6K_0	022726.448	−045159.520	−105	3	2020-10-07	2459125.32	3.5	summed to M6K_1
VVDS	M5H	022630.656	−044152.010	75	33	2020-10-08	2459130.46	2.8	6/7/12
VVDS	M5K	022630.656	−044152.010	75	33	2020-10-08	2459130.46	2.8	5/12/12
COSMOS	M7H	100016.331	+023959.780	145	36	2020-12-20	2459203.97	8.8	3/7/10
COSMOS	M7K	100016.331	+023959.780	145	37	2020-12-20	2459203.97	8.8	0/7/8
COSMOS	M6H	100200.465	+024022.660	180	36	2020-12-21	2459204.90	8.8	8/14/18
COSMOS	M6K	100200.465	+024022.660	180	36	2020-12-21	2459204.90	8.8	2/10/17
COSMOS	M8H	100057.749	+024042.990	55	30	2020-12-21	2459205.03	8.7	5/12/14
COSMOS	M8K	100057.749	+024042.990	55	30	2020-12-21	2459205.03	8.7	0/9/10
COSMOS	M10H	095928.310	+023020.540	70	28	2020-12-22	2459205.53	8.7	5/11/16
COSMOS	M10K	095928.310	+023020.540	70	28	2020-12-22	2459205.53	8.7	2/4/7
COSMOS	M9H	095936.806	+023227.230	230	35	2020-12-22	2459205.90	8.7	5/8/11
COSMOS	M9K	095936.806	+023227.230	230	36	2020-12-22	2459205.90	8.7	6/10/12
COSMOS	M11H	095953.706	+024016.910	145	36	2021-01-14	2459228.81	6.1	3/11/15
COSMOS	M11K	095953.706	+024016.910	145	36	2021-01-14	2459228.81	6.1	2/8/13
COSMOS	M12H	100144.876	+021013.710	175	36	2021-01-15	2459229.82	6.0	5/11/15
COSMOS	M12K	100144.876	+021013.710	175	36	2021-01-15	2459229.82	6.0	0/5/7
COSMOS	M13H	100112.552	+014557.890	85	36	2021-01-15	2459229.93	6.0	5/10/11
COSMOS	M7H	100016.331	+023959.780	145	36	2021-01-16	2459230.83	5.8	3/7/10
COSMOS	M7K	100016.331	+023959.780	145	36	2021-01-16	2459230.83	5.8	5/10/11
COSMOS	M8H	100200.465	+024022.660	180	40	2021-01-16	2459269.20	5.7	4/10/14
COSMOS	M8K	100200.465	+024022.660	180	40	2021-01-16	2459269.20	5.7	2/12/13
COSMOS	M14H	100135.484	+022000.480	160	36	2021-02-20	2459265.25	0.2	2/11/14

Table A.1. continued.

Field	Mask ID	RA_{cen} (hms)	Dec_{cen} (dms)	Rot.Angle deg	nExp (×200 s)	UT Date (yyy.mm.dd)	JD	$z_{helcorr}$ ($\times 10^5$)	Success Rate (Flag ≥ 3/Prim/Observed)
COSMOS	M14K	100135.484	+022000.480	160	37	2021-02-20	2459265.25	0.2	0/8/12
COSMOS	M15H	100145.151	+024022.550	115	36	2021-02-23	2459268.38	−0.3	3/14/17
COSMOS	M15K	100145.151	+024022.550	115	36	2021-02-23	2459268.38	−0.3	3/14/15
COSMOS	M17H	100112.883	+022431.600	140	36	2021-02-23	2459268.23	−0.4	6/14/17
COSMOS	M17K	100112.883	+022431.600	140	37	2021-02-23	2459268.23	−0.4	2/16/16
COSMOS	M18H	100120.693	+022216.430	105	27	2021-02-23	2459269.20	−0.5	4/12/14
COSMOS	M18K	100120.693	+022216.430	105	27	2021-02-24	2459269.20	−0.5	0/7/10
COSMOS	M20H	100016.511	+014607.640	150	36	2021-02-24	2459269.30	−0.5	5/11/14
COSMOS	M20K	100016.511	+014607.640	150	36	2021-02-24	2459269.30	−0.5	4/9/13
COSMOS	M22H	095944.102	+022014.340	30	31	2021-02-24	2459269.41	−0.5	1/10/15
COSMOS	M22K	095944.102	+022014.340	30	32	2021-02-24	2459269.41	−0.5	1/15/18
COSMOS	M23H	095912.153	+015008.170	90	23	2021-03-21	2459294.15	−4.6	3/11/15
COSMOS	M23K	095912.153	+015008.170	90	23	2021-03-21	2459294.15	−4.6	1/8/12
COSMOS	LAE3H	100025.092	+021627.160	0	19	2021-03-22	2459295.19	−4.7	0/6/6
COSMOS	LAE3K	100025.092	+021627.160	0	19	2021-03-22	2459295.19	−4.7	0/4/5
COSMOS	LAE4H	100041.352	+021239.210	−15	36	2021-03-23	2459296.18	−4.9	0/3/6
COSMOS	LAE4K	100041.352	+021239.210	−15	36	2021-03-23	2459296.18	−4.9	3/6/10
COSMOS	M24H	100153.446	+021613.970	100	15	2021-03-23	2459296.26	−4.8	0/9/15
COSMOS	M24K	100153.446	+021613.970	100	15	2021-03-23	2459296.26	−4.8	corrupted
COSMOS	M25H	095936.030	+020806.570	180	13	2021-03-27	2459301.35	−5.5	1/12/17
COSMOS	M25K	095936.030	+020806.570	180	13	2021-03-27	2459301.35	−5.5	0/17/17
COSMOS	M25H	095936.030	+020806.570	180	36	2021-04-20	2459324.24	−8.1	7/12/17
COSMOS	M25K	095936.030	+020806.570	180	36	2021-04-20	2459324.24	−8.1	4/17/17
COSMOS	M28H	095952.615	+015207.480	150	35	2021-04-24	2459328.19	−8.5	7/14/14
COSMOS	M28K	095952.615	+015207.480	150	35	2021-04-24	2459328.19	−8.5	1/14/14
COSMOS	M27H_1	095912.104	+022214.200	140	16	2021-04-22	2459328.28	−8.5	6/13/14
COSMOS	M27H_2	095912.104	+022214.200	140	16	2021-04-23	2459328.28	−8.5	summed to M27H_1
COSMOS	M27K_1	095912.104	+022214.200	140	16	2021-04-22	2459328.28	−8.5	corrupted
COSMOS	M27K_2	095912.104	+022214.200	140	16	2021-04-23	2459328.28	−8.5	2/6/10
COSMOS	M29H	095912.178	+021414.250	15	36	2021-04-25	2459329.20	−8.6	4/11/13
COSMOS	M29K	095912.178	+021414.250	15	36	2021-04-25	2459329.20	−8.6	2/13/13
COSMOS	M24H	100153.446	+021613.970	100	10	2021-04-25	2459329.28	−8.5	4/9/15
COSMOS	M24K	100153.446	+021613.970	100	10	2021-04-25	2459329.28	−8.5	1/14/14
COSMOS	M19H	100104.598	+014801.750	135	32	2021-05-19	2459328.28	−9.6	4/12/15
COSMOS	M19K	100104.598	+014801.750	135	34	2021-05-19	2459328.28	−9.6	0/15/15

Appendix B: Table B.1

Table B.1. Sample of galaxies with good spectroscopic redshifts. The explanation of the different columns is given in Sect. 4.

OBJ_ID	RA	Dec	z_{spec}	Flag	Line	1D-Spectrum
13275	150.3162252	1.7379527	2.4078	4.0	[O III]	COSMOS_LBT_JAN21_1d_13275_M13Hsky_S21
20825	150.0527463	1.7531398	1.6520	4.0	Hα	COSMOS_LBT_FEB21_1d_20825_M20Hsky_S08
21075	150.2729757	1.7538638	1.5172	3.0	Hα	COSMOS_LBT_JAN21_1d_21075_M13Hsky_S13
21964	150.0395616	1.7555454	2.5610	3.0	[O III]	COSMOS_LBT_FEB21_1d_21964_M20Hsky_S19
26585	150.079045	1.7650675	2.3980	4.0	Hα	COSMOS_LBT_FEB21_1d_26585_M20Ksky_S16
28028	150.3115341	1.7680673	1.5573	3.5	Hα	COSMOS_LBT_JAN21_1d_28028_M13Hsky_S17
31318	150.0632315	1.7735528	2.2090	3.0	Hα	COSMOS_LBT_FEB21_1d_31318_M20Ksky_S11
31613	150.2616012	1.7747734	2.2790	4.0	[O III]	COSMOS_LBT_MAY21_1d_31613_M19Hsky_S17
32792	150.0340033	1.7783992	2.3520	3.0	Hα	COSMOS_LBT_FEB21_1d_32792_M20Ksky_S14
32961	150.281817	1.778883	1.4621	4.0	Hα	COSMOS_LBT_JAN21_1d_32961_M13Hsky_S14
32961	150.281817	1.778883	1.4626	3.5	Hα	COSMOS_LBT_MAY21_1d_32961_M19Hsky_S08
33981	150.0619008	1.7806075	1.6460	4.0	Hα	COSMOS_LBT_FEB21_1d_33981_M20Hsky_S17
34952	150.2745122	1.7830993	1.4406	3.0	Hα	COSMOS_LBT_JAN21_1d_34952_M13Hsky_S12
35658	150.0938201	1.7841196	1.4990	4.0	Hα	COSMOS_LBT_FEB21_1d_35658_M20Hsky_S12
38008	150.2506447	1.7882888	1.5028	3.0	Hα	COSMOS_LBT_MAY21_1d_38008_M19Hsky_S18
38150	150.0593597	1.788839	2.3940	4.0	[O III]	COSMOS_LBT_FEB21_1d_38150_M20Hsky_S21
38150	150.0593597	1.788839	2.3950	3.0	Hα	COSMOS_LBT_FEB21_1d_38150_M20Ksky_S13
51484	149.7970089	1.8136581	1.6334	3.5	Hα	COSMOS_LBT_MAR21_1d_51484_M23Hsky_S15
53612	149.7731289	1.8199504	1.5079	3.0	Hα	COSMOS_LBT_MAR21_1d_53612_M23Hsky_S13
55494	150.292338	1.8234505	1.3193	4.0	Hα	COSMOS_LBT_MAY21_1d_55494_M19Hsky_S09
63116	149.9518298	1.8386457	1.6518	3.5	Hα	COSMOS_LBT_APR21_1d_63116_M28Hsky_S21
63265	149.9568087	1.8382493	1.6498	4.0	Hα	COSMOS_LBT_APR21_1d_63265_M28Hsky_S09
63462	149.9680223	1.8398813	1.6498	3.5	Hα	COSMOS_LBT_APR21_1d_63462_M28Hsky_S10
63645	149.7895905	1.8398429	1.4849	3.0	Hα	COSMOS_LBT_MAR21_1d_63645_M23Hsky_S14
71209	149.7748281	1.8565425	2.5118	3.0	Hα	COSMOS_LBT_MAR21_1d_71209_M23Ksky_S13
72589	149.9614682	1.860202	1.5558	4.0	Hα	COSMOS_LBT_APR21_1d_72589_M28Hsky_S20
72810	150.0038562	1.8537445	2.5107	3.0	Hα	COSMOS_LBT_APR21_1d_72810_M28Ksky_S09
76300	149.9797066	1.8673859	1.4198	3.0	Hα	COSMOS_LBT_APR21_1d_76300_M28Hsky_S08
76722	149.9897509	1.8677315	1.3573	3.0	Hα	COSMOS_LBT_APR21_1d_76722_M28Hsky_S15
91047	149.9912965	1.8967987	1.4948	3.0	Hα	COSMOS_LBT_APR21_1d_91047_M28Hsky_S16
100154	149.6682826	1.915744	1.4394	3.0	Hα	COSMOS_LBT_MAR20_1d_100154_M1Hsky_S09
109400	149.6567535	1.9354134	1.6336	3.0	Hα	COSMOS_LBT_MAR20_1d_109400_M1Hsky_S12
110669	149.6868649	1.9363752	1.6411	3.5	Hα	COSMOS_LBT_MAR20_1d_110669_M1Hsky_S08
111064	149.6323822	1.9393212	1.6164	3.5	Hα	COSMOS_LBT_MAR20_1d_111064_M1Hsky_S15
115146	149.6558387	1.9476929	2.5189	3.0	Hα	COSMOS_LBT_MAR20_1d_115146_M1Ksky_S14
116202	149.6839698	1.9502112	1.5329	3.5	Hα	COSMOS_LBT_MAR20_1d_116202_M1Hsky_S13
121050	149.6511528	1.961198	1.5708	3.0	Hα	COSMOS_LBT_MAR20_1d_121050_M1Hsky_S16
121736	149.6605124	1.9621859	2.1603	3.0	Hα	COSMOS_LBT_MAR20_1d_121736_M1Ksky_S17
193269	149.9183382	2.1055916	1.3605	3.0	Hα	COSMOS_LBT_APR21_1d_193269_M25Hsky_S15
194648	149.7419169	2.1075764	1.5313	3.0	Hα	COSMOS_LBT_MAR20_1d_194648_M3Hsky_S10
197419	149.9092285	2.1130251	1.4708	3.0	Hα	COSMOS_LBT_APR21_1d_197419_M25Hsky_S08
199380	149.9150387	2.1170209	2.2631	4.0	Hα	COSMOS_LBT_APR21_1d_199380_M25Ksky_S09
201260	149.8729828	2.1204449	2.3737	3.0	Hα	COSMOS_LBT_APR21_1d_201260_M25Ksky_S08
202778	149.8772597	2.1237659	1.5083	3.5	Hα	COSMOS_LBT_APR21_1d_202778_M25Hsky_S17
209194	149.7100321	2.136129	2.3874	3.0	[O III]	COSMOS_LBT_MAR20_1d_209194_M3Hsky_S22
209927	149.9253192	2.134973	1.6063	3.0	Hα	COSMOS_LBT_APR21_1d_209927_M25Hsky_S22
210275	150.4068985	2.1383306	1.6417	3.0	Hα	COSMOS_LBT_JAN21_1d_210275_M12Hsky_S11
211581	149.7091359	2.1392878	1.6414	3.5	Hα	COSMOS_LBT_MAR20_1d_211581_M3Hsky_S14
211984	149.8673655	2.1410346	2.4487	4.0	[O III]	COSMOS_LBT_APR21_1d_211984_M25Hsky_S18
215091	149.9281427	2.1470197	2.3757	3.0	Hα	COSMOS_LBT_APR21_1d_215091_M25Ksky_S21
217459	149.7618337	2.1518038	1.6168	3.0	Hα	COSMOS_LBT_MAR20_1d_217459_M3Hsky_S08
218192	149.904775	2.15362	2.3852	4.0	Hα	COSMOS_LBT_APR21_1d_218192_M25Ksky_S11
218228	149.717966	2.1530929	2.4342	3.5	[O III]	COSMOS_LBT_MAR20_1d_218228_M3Hsky_S21

Table B.1. continued.

OBJ_ID	RA	Dec	z_{spec}	Flag	Line	1D-Spectum
218763	149.7468821	2.1537101	1.6377	3.0	Hα	COSMOS_LBT_MAR20_1d_218763_M3Hsky_S17
219390	149.7583034	2.1559746	1.5267	3.0	Hα	COSMOS_LBT_MAR20_1d_219390_M3Hsky_S18
220827	150.4434614	2.1586643	1.5392	4.0	Hα	COSMOS_LBT_JAN21_1d_220827_M12Hsky_S10
221149	150.4139644	2.1591002	1.5572	4.0	Hα	COSMOS_LBT_JAN21_1d_221149_M12Hsky_S09
223074	149.8970859	2.1622611	2.2388	3.0	[O III]	COSMOS_LBT_MAR21_1d_223074_M25Hsky_S20
224872	149.8749001	2.1660171	1.5268	3.0	Hα	COSMOS_LBT_APR21_1d_224872_M25Hsky_S12
226236	149.7460689	2.1675662	2.4344	4.0	Hα	COSMOS_LBT_MAR20_1d_226236_M3Ksky_S17
226249	150.4191533	2.1687531	1.5962	3.5	Hα	COSMOS_LBT_JAN21_1d_226249_M12Hsky_S19
234751	150.4445932	2.1847414	1.5192	3.0	Hα	COSMOS_LBT_JAN21_1d_234751_M12Hsky_S13
248229	150.1880526	2.2102579	2.4808	3.0	Hα	COSMOS_LBT_MAR21_1d_248229_LAE4Ksky_S13
251341	149.7751888	2.216971	2.3177	4.0	Hα	COSMOS_LBT_APR21_1d_251341_M29Ksky_S12
251539	149.825632	2.217383	2.4540	4.0	[O III]	COSMOS_LBT_APR21_1d_251539_M29Hsky_S20
253054	149.7693121	2.2208096	1.4158	4.0	Hα	COSMOS_LBT_APR21_1d_253054_M29Hsky_S14
254879	150.0895379	2.2235747	1.3521	3.0	Hα	COSMOS_LBT_MAR20_1d_254879_M2Hsky_S17
256237	149.8125082	2.2260419	1.5503	4.0	Hα	COSMOS_LBT_APR21_1d_256237_M29Hsky_S16
261029	149.8140962	2.234968	1.6858	3.5	Hα	COSMOS_LBT_APR21_1d_261029_M29Hsky_S17
261242	150.1912935	2.2358824	2.2798	4.0	Hα	COSMOS_LBT_MAR21_1d_261242_LAE4Ksky_S21
263941	149.802669	2.2413337	2.2147	3.5	Hα	COSMOS_LBT_APR21_1d_263941_M29Ksky_S08
272390	150.4427008	2.2577357	1.5845	4.0	Hα	COSMOS_LBT_APR21_1d_272390_M24Hsky_S15
277689	150.4825951	2.2692277	1.5850	4.0	Hα	COSMOS_LBT_APR21_1d_277689_M24Hsky_S10
281625	150.489104	2.2775923	1.6303	4.0	Hα	COSMOS_LBT_APR21_1d_281625_M24Hsky_S11
305682	149.9338397	2.325281	1.6150	3.0	Hα	COSMOS_LBT_FEB21_1d_305682_M22Hsky_S14
311645	149.7982448	2.3368401	1.6048	3.0	Hα	COSMOS_LBT_APR21_1d_311645_M27Hsky_S15
315750	150.3914582	2.3435241	1.4790	3.0	Hα	COSMOS_LBT_FEB21_1d_315750_M14Hsky_S09
320989	149.8092325	2.3544984	2.3707	3.0	[O III]	COSMOS_LBT_APR21_1d_320989_M27Hsky_S21
321846	150.3609407	2.3563503	1.5855	3.5	Hα	COSMOS_LBT_FEB21_1d_321846_M18Hsky_S21
323850	149.9217085	2.3597902	2.1015	4.0	Hα	COSMOS_LBT_FEB21_1d_323850_M22Ksky_S09
326545	150.3990555	2.3652568	1.4830	3.0	Hα	COSMOS_LBT_FEB21_1d_326545_M14Hsky_S08
328061	150.3336896	2.3676283	1.6350	3.0	Hα	COSMOS_LBT_FEB21_1d_328061_M18Hsky_S14
329209	150.338739	2.3703542	1.5800	3.0	Hα	COSMOS_LBT_FEB21_1d_329209_M18Hsky_S09
330051	149.8129738	2.3717757	1.6053	3.0	Hα	COSMOS_LBT_APR21_1d_330051_M27Hsky_S08
331551	149.804426	2.3743435	1.6261	3.5	Hα	COSMOS_LBT_APR21_1d_331551_M27Hsky_S17
331974	149.791189	2.3754079	1.4323	3.0	Hα	COSMOS_LBT_APR21_1d_331974_M27Hsky_S10
332036	149.7654438	2.3750567	1.5273	3.0	Hα	COSMOS_LBT_APR21_1d_332036_M27Hsky_S13
334638	150.3069896	2.3796186	1.5800	4.0	Hα	COSMOS_LBT_FEB21_1d_334638_M17Hsky_S19
336706	150.3182657	2.383641	1.3850	3.0	Hα	COSMOS_LBT_FEB21_1d_336706_M17Hsky_S09
340178	150.3197125	2.3908843	2.5510	3.0	Hα	COSMOS_LBT_FEB21_1d_340178_M17Ksky_S11
344560	150.3518992	2.4002879	1.4320	4.0	Hα	COSMOS_LBT_FEB21_1d_344560_M18Hsky_S18
346399	150.2869306	2.4032503	1.4390	3.0	Hα	COSMOS_LBT_FEB21_1d_346399_M17Hsky_S14
347369	150.2775421	2.4062789	1.5020	4.0	Hα	COSMOS_LBT_FEB21_1d_347369_M17Hsky_S10
348742	150.3284294	2.4085777	1.4830	3.0	Hα	COSMOS_LBT_FEB21_1d_348742_M17Hsky_S08
349330	150.3218736	2.4103132	2.4720	3.5	Hα	COSMOS_LBT_FEB21_1d_349330_M17Ksky_S08
385760	149.8700627	2.4886839	1.5598	3.5	Hα	COSMOS_LBT_DEC20_1d_385760_M10Hsky_S18
400371	149.8867628	2.5176858	1.5830	3.5	Hα	COSMOS_LBT_DEC20_1d_400371_M9Hsky_S14
402003	149.8499016	2.5216286	1.6036	3.0	Hα	COSMOS_LBT_DEC20_1d_402003_M10Hsky_S24
402635	149.8462499	2.5224695	2.1713	3.0	[O III]	COSMOS_LBT_DEC20_1d_402635_M10Hsky_S19
402635	149.8462499	2.5224695	2.1703	4.0	Hα	COSMOS_LBT_DEC20_1d_402635_M10Ksky_S12
404898	149.9153074	2.5273345	2.2453	3.5	Hα	COSMOS_LBT_DEC20_1d_404898_M9Ksky_S10
406056	149.9333663	2.5297759	2.4252	3.0	Hα	COSMOS_LBT_DEC20_1d_406056_M9Ksky_S12
406594	149.8966304	2.5305503	2.2363	3.0	Hα	COSMOS_LBT_DEC20_1d_406594_M9Ksky_S15
407529	149.8794106	2.5322392	1.5838	3.0	Hα	COSMOS_LBT_DEC20_1d_407529_M10Hsky_S20
409697	149.9326151	2.5364134	2.2453	4.0	Hα	COSMOS_LBT_DEC20_1d_409697_M9Ksky_S13
412341	149.8873947	2.5422249	2.2493	4.0	[O III]	COSMOS_LBT_DEC20_1d_412341_M10Hsky_S21
417124	149.9357984	2.5514111	2.1963	3.0	[O III]	COSMOS_LBT_DEC20_1d_417124_M9Hsky_S19
421534	149.919234	2.5604157	2.3243	4.0	Hα	COSMOS_LBT_DEC20_1d_421534_M9Ksky_S14

Table B.1. continued.

OBJ_ID	RA	Dec	z_{spec}	Flag	Line	1D-Spectum
423163	149.9075378	2.5636165	1.5572	3.0	Hα	COSMOS_LBT_DEC20_1d_423163_M9Hsky_S22
426464	149.8888229	2.569995	1.6652	3.5	Hα	COSMOS_LBT_DEC20_1d_426464_M9Hsky_S17
427350	149.9084958	2.5712201	1.6607	3.0	Hα	COSMOS_LBT_DEC20_1d_427350_M9Hsky_S13
459855	150.0530532	2.6369884	1.4466	3.0	Hα	COSMOS_LBT_JAN21_1d_459855_M7Hsky_S10
462025	150.0826055	2.6413449	2.0873	3.0	[O III]	COSMOS_LBT_DEC20_1d_462025_M7Hsky_S15
462025	150.0826055	2.6413449	2.0877	3.0	[O III]	COSMOS_LBT_JAN21_1d_462025_M7Hsky_S15
463893	150.4854222	2.6455409	2.3473	4.0	[O III]	COSMOS_LBT_DEC20_1d_463893_M6Hsky_S24
463893	150.4854222	2.6455409	2.3473	3.0	Hα	COSMOS_LBT_DEC20_1d_463893_M6Ksky_S14
465574	150.4536772	2.6487302	2.4120	3.0	Hα	COSMOS_LBT_FEB21_1d_465574_M15Ksky_S15
468350	150.48936	2.6544405	2.3955	3.0	Hα	COSMOS_LBT_DEC20_1d_468350_M6Ksky_S13
472716	150.2653786	2.6627636	1.7120	3.5	Hα	COSMOS_LBT_DEC20_1d_472716_M8Hsky_S16
472716	150.2653786	2.6627636	1.7122	3.0	Hα	COSMOS_LBT_JAN21_1d_472716_M8Hsky_S16
474523	150.0922862	2.6656468	2.2117	3.5	Hα	COSMOS_LBT_JAN21_1d_474523_M7Ksky_S09
475417	150.0911944	2.6683391	2.5042	3.0	Hα	COSMOS_LBT_JAN21_1d_475417_M7Ksky_S18
475527	150.0591837	2.6685413	2.4372	4.0	Hα	COSMOS_LBT_JAN21_1d_475527_M7Ksky_S11
476044	149.9910794	2.6692601	1.5645	4.0	Hα	COSMOS_LBT_JAN21_1d_476044_M11Hsky_S15
476459	150.4419312	2.6701195	1.6134	3.5	Hα	COSMOS_LBT_FEB21_1d_476459_M15Hsky_S20
476771	150.5134492	2.66873	1.5792	3.0	Hα	COSMOS_LBT_DEC20_1d_476771_M6Hsky_S21
478878	150.4690208	2.675255	1.6122	3.0	Hα	COSMOS_LBT_DEC20_1d_478878_M6Hsky_S25
479007	150.0857052	2.6747758	2.2723	4.0	[O III]	COSMOS_LBT_DEC20_1d_479007_M7Hsky_S16
479007	150.0857052	2.6747758	2.2722	4.0	[O III]	COSMOS_LBT_JAN21_1d_479007_M7Hsky_S16
479007	150.0857052	2.6747758	2.2730	4.0	Hα	COSMOS_LBT_JAN21_1d_479007_M7Ksky_S08
480046	150.056362	2.6768332	2.2702	4.0	Hα	COSMOS_LBT_JAN21_1d_480046_M7Ksky_S15
480239	150.2307456	2.6769689	1.5994	3.0	Hα	COSMOS_LBT_DEC20_1d_480239_M8Hsky_S09
480640	150.5207857	2.6781376	1.5732	3.5	Hα	COSMOS_LBT_DEC20_1d_480640_M6Hsky_S13
481315	150.2668853	2.67968	2.4913	4.0	[O III]	COSMOS_LBT_DEC20_1d_481315_M8Hsky_S19
481315	150.2668853	2.67968	2.4907	4.0	[O III]	COSMOS_LBT_JAN21_1d_481315_M8Hsky_S19
481317	150.4749598	2.6794807	1.5390	3.0	Hα	COSMOS_LBT_FEB21_1d_481317_M15Hsky_S12
481647	150.2672757	2.6799633	1.5010	4.0	Hα	COSMOS_LBT_DEC20_1d_481647_M8Hsky_S19
481647	150.2672757	2.6799633	1.5010	4.0	Hα	COSMOS_LBT_JAN21_1d_481647_M8Hsky_S19
482104	150.4218192	2.681305	2.1450	3.0	[O III]	COSMOS_LBT_FEB21_1d_482104_M15Hsky_S18
483394	150.5219636	2.6838403	2.2158	4.0	[O III]	COSMOS_LBT_DEC20_1d_483394_M6Hsky_S20
483647	150.2127732	2.6836628	2.2242	3.0	Hα	COSMOS_LBT_JAN21_1d_483647_M8Ksky_S17
484275	149.9975234	2.6859328	2.0482	3.0	[O III]	COSMOS_LBT_JAN21_1d_484275_M11Hsky_S19
484310	150.2587791	2.6852644	1.5882	3.5	Hα	COSMOS_LBT_DEC20_1d_484310_M8Hsky_S22
484310	150.2587791	2.6852644	1.5876	3.0	Hα	COSMOS_LBT_JAN21_1d_484310_M8Hsky_S22
484662	150.0656512	2.6864807	1.4061	3.0	Hα	COSMOS_LBT_DEC20_1d_484662_M7Hsky_S11
486496	150.5087376	2.7042991	1.5354	3.5	Hα	COSMOS_LBT_DEC20_1d_486496_M6Hsky_S15
486866	149.967041	2.6964446	1.4401	3.5	Hα	COSMOS_LBT_JAN21_1d_486866_M11Hsky_S14
489100	150.4748461	2.6867608	1.6377	4.0	Hα	COSMOS_LBT_DEC20_1d_489100_M6Hsky_S17
489314	149.9812037	2.6941987	2.2162	3.0	Hα	COSMOS_LBT_JAN21_1d_489314_M11Ksky_S19
490030	149.9783643	2.7028003	2.3922	4.0	Hα	COSMOS_LBT_JAN21_1d_490030_M11Ksky_S12
492453	150.2442763	2.7067051	2.4702	3.0	Hα	COSMOS_LBT_JAN21_1d_492453_M8Ksky_S20
494350	150.4846551	2.6939799	1.6412	3.0	Hα	COSMOS_LBT_DEC20_1d_494350_M6Hsky_S14
549854	149.907150209	2.137621434	1.4802	3.0	Hα	COSMOS_LBT_APR21_1d_549854_M25Hsky_S10
603116	150.197082912	2.21687046	2.4638	4.0	Hα	COSMOS_LBT_MAR21_1d_603116_LAE4Ksky_S19
621780	150.471209414	2.2446394	2.4847	4.0	Hα	COSMOS_LBT_APR21_1d_621780_M24Ksky_S08
646613	150.468731703	2.281641135	1.4908	3.0	Hα	COSMOS_LBT_APR21_1d_646613_M24Hsky_S12
703468	149.78839164	2.36554692	2.3277	3.0	Hα	COSMOS_LBT_APR21_1d_703468_M27Ksky_S09
720513	149.803548302	2.391162136	2.2512	4.0	Hα	COSMOS_LBT_APR21_1d_720513_M27Ksky_S13
732820	150.302551814	2.411721348	1.6495	3.0	Hα	COSMOS_LBT_FEB21_1d_732820_M17Hsky_S13
811438	149.876631272	2.530976324	2.3623	3.0	Hα	COSMOS_LBT_DEC20_1d_811438_M9Ksky_S18
811438	149.876631272	2.530976324	2.3618	3.0	Hα	COSMOS_LBT_DEC20_1d_811438_M10Ksky_S15
911024	150.434047436	2.68423913	2.2965	3.0	Hα	COSMOS_LBT_FEB21_1d_911024_M15Ksky_S18
914020	150.445804162	2.685678498	1.5730	3.0	Pa	COSMOS_LBT_FEB21_1d_914020_M15Ksky_S24

Table B.1. continued.

OBJ_ID	RA	Dec	z_{spec}	Flag	Line	1D-Spectum
3324	36.6244607	−4.9884302	1.5340	4.0	Hα	VVDS_LBT_OCT20_1d_3324_M3Hsky_S16
3324	36.6244607	−4.9884302	1.5339	4.0	Hα	VVDS_LBT_OCT19_1d_3324_M3Hsky_S16
6892	36.5680458	−4.9803015	2.2071	3.0	[O III]	VVDS_LBT_OCT19_1d_6892_M3Hsky_S21
7941	36.6288502	−4.9780309	1.5346	3.0	Hα	VVDS_LBT_OCT20_1d_7941_M3Hsky_S17
7941	36.6288502	−4.9780309	1.5346	3.5	Hα	VVDS_LBT_OCT19_1d_7941_M3Hsky_S17
15031	36.509626	−4.9637322	2.0701	3.0	[O III]	VVDS_LBT_OCT20_1d_15031_M4Hsky_S23
19965	36.5629042	−4.9542579	1.5200	3.5	Hα	VVDS_LBT_OCT19_1d_19965_M1Hsky_S17
21178	36.5418393	−4.9519901	1.5304	3.0	Hα	VVDS_LBT_OCT19_1d_21178_M1Hsky_S16
21370	36.5334932	−4.9518214	2.3841	3.0	Hα	VVDS_LBT_OCT20_1d_21370_M4Ksky_S13
22805	36.528381	−4.9487815	1.5334	3.0	Hα	VVDS_LBT_OCT20_1d_22805_M4Hsky_S16
22805	36.528381	−4.9487815	1.5331	3.5	Hα	VVDS_LBT_OCT19_1d_22805_M4Hsky_S16
24882	36.5648159	−4.94453	1.3761	4.0	Hα	VVDS_LBT_OCT20_1d_24882_M3Hsky_S11
24882	36.5648159	−4.94453	1.3761	3.0	Hα	VVDS_LBT_OCT19_1d_24882_M1Hsky_S18
24882	36.5648159	−4.94453	1.3766	3.0	Hα	VVDS_LBT_OCT19_1d_24882_M3Hsky_S11
24903	36.5064947	−4.9450216	1.5781	3.0	Hα	VVDS_LBT_OCT20_1d_24903_M4Hsky_S21
24903	36.5064947	−4.9450216	1.5781	3.0	Hα	VVDS_LBT_OCT19_1d_24903_M4Hsky_S21
29861	36.59385	−4.9345849	2.0941	3.5	Hα	VVDS_LBT_OCT20_1d_29861_M3Ksky_S20
30293	36.582892	−4.9341326	1.5335	4.0	Hα	VVDS_LBT_OCT19_1d_30293_M1Hsky_S11
34978	36.6069178	−4.9249799	1.5624	4.0	Hα	VVDS_LBT_OCT19_1d_34978_M2Hsky_S16
36412	36.587422	−4.922475	1.5366	4.0	Hα	VVDS_LBT_OCT19_1d_36412_M1Hsky_S20
36412	36.587422	−4.922475	1.5366	4.0	Hα	VVDS_LBT_OCT19_1d_36412_M2Hsky_S15
37921	36.493333	−4.9206908	2.0007	3.0	[O III]	VVDS_LBT_OCT20_1d_37921_M4Hsky_S24
37921	36.493333	−4.9206908	2.0006	4.0	[O III]	VVDS_LBT_OCT19_1d_37921_M4Hsky_S24
38524	36.6009144	−4.9185782	1.5464	3.0	Hα	VVDS_LBT_OCT19_1d_38524_M2Hsky_S13
39192	36.5348629	−4.9172989	2.0604	4.0	[O III]	VVDS_LBT_OCT19_1d_39192_M1Hsky_S22
40659	36.4435417	−4.9146046	1.6057	4.0	Hα	VVDS_LBT_JAN20_1d_40659_M9Hsky_S14
44310	36.5107537	−4.9075348	1.3711	3.5	Hα	VVDS_LBT_OCT19_1d_44310_M4Hsky_S12
45642	36.517377	−4.9061548	2.0616	4.0	Hα	VVDS_LBT_OCT20_1d_45642_M4Ksky_S20
47083	36.4888123	−4.9021975	1.6245	4.0	Hα	VVDS_LBT_JAN20_1d_47083_M9Hsky_S17
49143	36.4810046	−4.8989504	2.4147	4.0	[O III]	VVDS_LBT_JAN20_1d_49143_M9Hsky_S11
50696	36.5757347	−4.8950953	1.5200	3.5	Hα	VVDS_LBT_OCT19_1d_50696_M2Hsky_S17
51100	36.4519719	−4.8943098	1.5836	3.0	Hα	VVDS_LBT_JAN20_1d_51100_M9Hsky_S12
52018	36.6037449	−4.8923901	1.6183	3.5	Hα	VVDS_LBT_OCT19_1d_52018_M2Hsky_S18
54789	36.8943492	−4.8870347	1.4426	3.0	Hα	VVDS_LBT_OCT20_1d_54789_M6Hsky_S14
55141	36.4425414	−4.8865782	2.2326	3.0	Hα	VVDS_LBT_JAN20_1d_55141_M9Ksky_S17
56255	36.6051263	−4.8844258	1.5303	4.0	Hα	VVDS_LBT_OCT19_1d_56255_M2Hsky_S12
56891	36.5720134	−4.884359	2.2711	3.0	[O III]	VVDS_LBT_OCT19_1d_56891_M2Hsky_S19
57263	36.8684341	−4.882315	2.2801	3.0	Hα	VVDS_LBT_OCT20_1d_57263_M6Ksky_S11
64030	36.8392892	−4.8692322	2.3328	3.0	Hα	VVDS_LBT_OCT20_1d_64030_M6Ksky_S17
66084	36.8538979	−4.8654714	2.2856	4.0	[O III]	VVDS_LBT_OCT20_1d_66084_M6Hsky_S21
68382	36.8625965	−4.863006	1.5341	3.5	Hα	VVDS_LBT_OCT20_1d_68382_M6Hsky_S17
68592	36.4582577	−4.8616541	1.5203	3.0	Hα	VVDS_LBT_JAN20_1d_68592_M9Hsky_S18
68635	36.4673469	−4.8614609	2.2052	4.0	[O III]	VVDS_LBT_JAN20_1d_68635_M9Hsky_S24
77168	36.8614225	−4.8455261	1.5259	3.5	Hα	VVDS_LBT_OCT20_1d_77168_M6Hsky_S13
125460	36.118401	−4.7518593	1.4856	4.0	Hα	VVDS_LBT_OCT20_1d_125460_M13Hsky_S16
125920	36.1522153	−4.7512865	1.7006	3.0	Hα	VVDS_LBT_OCT20_1d_125920_M13Hsky_S15
127119	36.1466843	−4.7480526	2.1141	3.0	Hα	VVDS_LBT_OCT20_1d_127119_M13Ksky_S16
128166	36.1172243	−4.7457655	2.0408	3.0	Hα	VVDS_LBT_OCT20_1d_128166_M13Ksky_S11
135766	36.0902942	−4.7310129	2.2975	4.0	Hα	VVDS_LBT_OCT20_1d_135766_M13Ksky_S14
137799	36.1486107	−4.7260611	2.2142	3.0	Hα	VVDS_LBT_OCT20_1d_137799_M13Ksky_S15
138587	36.1042005	−4.7247136	1.6776	3.0	Hα	VVDS_LBT_OCT20_1d_138587_M13Hsky_S12
138945	36.5706378	−4.7236601	2.2062	3.0	Hα	VVDS_LBT_OCT20_1d_138945_M5Ksky_S17
140031	36.0898178	−4.7212704	2.2141	4.0	[O III]	VVDS_LBT_OCT20_1d_140031_M13Hsky_S19

Table B.1. continued.

OBJ_ID	RA	Dec	z_{spec}	Flag	Line	1D-Spectum
140031	36.0898178	−4.7212704	2.2141	3.0	Hα	VVDS_LBT_OCT20_1d_140031_M13Ksky_S18
140527	36.635215	−4.7209197	2.1296	3.0	Hα	VVDS_LBT_OCT20_1d_140527_M5Ksky_S21
142226	36.6331479	−4.7173309	1.5164	3.0	Hα	VVDS_LBT_OCT20_1d_142226_M5Hsky_S15
142226	36.6331479	−4.7173309	1.5166	4.0	Hα	VVDS_LBT_OCT19_1d_142226_M5Hsky_S15
144923	36.2271709	−4.7120479	1.5601	3.0	Hα	VVDS_LBT_OCT20_1d_144923_M5Hsky_S14
144923	36.2271709	−4.7120479	1.5600	4.0	Hα	VVDS_LBT_OCT19_1d_144923_M5Hsky_S14
147228	36.1020614	−4.7087143	1.5386	3.0	Hα	VVDS_LBT_OCT20_1d_147228_M13Hsky_S13
154912	36.34384	−4.6933544	2.1396	4.0	Hα	VVDS_LBT_OCT20_1d_154912_M11Ksky_S14
158984	36.3422744	−4.6854868	2.1911	3.5	Hα	VVDS_LBT_OCT20_1d_158984_M11Ksky_S12
160224	36.6517582	−4.6828961	1.6061	3.0	Hα	VVDS_LBT_OCT20_1d_160224_M5Hsky_S11
160224	36.6517582	−4.6828961	1.6061	4.0	Hα	VVDS_LBT_OCT20_1d_160224_M14Hsky_S12
160224	36.6517582	−4.6828961	1.6061	4.0	Hα	VVDS_LBT_OCT19_1d_160224_M5Hsky_S11
162982	36.6420709	−4.6787762	2.2448	4.0	Hα	VVDS_LBT_OCT20_1d_162982_M5Ksky_S12
162982	36.6420709	−4.6787762	2.2435	4.0	[O III]	VVDS_LBT_OCT19_1d_162982_M5Hsky_S20
163515	36.6101764	−4.6765857	1.5716	4.0	Hα	VVDS_LBT_OCT20_1d_163515_M5Hsky_S16
163515	36.6101764	−4.6765857	1.5716	3.0	Hα	VVDS_LBT_OCT20_1d_163515_M14Hsky_S15
163515	36.6101764	−4.6765857	1.5717	3.5	Hα	VVDS_LBT_OCT19_1d_163515_M5Hsky_S16
165659	36.3549882	−4.6723701	2.1395	3.0	[O III]	VVDS_LBT_OCT20_1d_165659_M11Hsky_S19
165659	36.3549882	−4.6723701	2.1396	4.0	Hα	VVDS_LBT_OCT20_1d_165659_M11Ksky_S11
165940	36.6296705	−4.671717	2.2646	4.0	Hα	VVDS_LBT_OCT20_1d_165940_M5Ksky_S20
165940	36.6296705	−4.671717	2.2651	3.0	Hα	VVDS_LBT_OCT20_1d_165940_M14Ksky_S19
166946	36.3469914	−4.669578	2.2211	3.5	Hα	VVDS_LBT_OCT20_1d_166946_M11Ksky_S15
167263	36.6519619	−4.6694611	2.2601	3.0	Hα	VVDS_LBT_OCT20_1d_167263_M5Ksky_S13
167263	36.6519619	−4.6694611	2.2596	4.0	Hα	VVDS_LBT_OCT20_1d_167263_M14Ksky_S13
167264	36.6445147	−4.6690833	2.2581	3.0	[O III]	VVDS_LBT_OCT20_1d_167264_M5Hsky_S19
167264	36.6445147	−4.6690833	2.2601	3.0	[O III]	VVDS_LBT_OCT19_1d_167264_M5Hsky_S19
168107	36.650895	−4.668188	1.5596	3.0	Hα	VVDS_LBT_OCT20_1d_168107_M5Hsky_S13
168107	36.650895	−4.668188	1.5601	3.0	Hα	VVDS_LBT_OCT19_1d_168107_M5Hsky_S13
168869	36.6114714	−4.6661429	2.4436	4.0	[O III]	VVDS_LBT_OCT20_1d_168869_M14Hsky_S21
168869	36.6114714	−4.6661429	2.4429	3.0	Hα	VVDS_LBT_OCT20_1d_168869_M14Ksky_S15
170223	36.3308287	−4.6636302	2.2088	3.0	[O III]	VVDS_LBT_OCT20_1d_170223_M11Hsky_S17
171656	36.638702	−4.6610195	2.2376	3.0	[O III]	VVDS_LBT_OCT20_1d_171656_M14Hsky_S19
171656	36.638702	−4.6610195	2.2375	3.0	Hα	VVDS_LBT_OCT20_1d_171656_M14Ksky_S21
171798	36.6554476	−4.6607726	2.2481	3.0	Hα	VVDS_LBT_OCT20_1d_171798_M14Ksky_S20
172082	36.6448409	−4.660273	1.5301	3.0	Hα	VVDS_LBT_OCT20_1d_172082_M8Hsky_S16
172693	36.6565846	−4.659415	1.4361	4.0	Hα	VVDS_LBT_OCT20_1d_172693_M8Hsky_S13
174768	36.6440171	−4.654438	1.6161	3.5	Hα	VVDS_LBT_OCT20_1d_174768_M14Hsky_S13
176272	36.319106	−4.6532566	1.5617	3.5	Hα	VVDS_LBT_OCT20_1d_176272_M11Hsky_S14
178570	36.6703436	−4.6478391	1.4899	3.5	Hα	VVDS_LBT_OCT20_1d_178570_M8Hsky_S11
178934	36.3514434	−4.6468935	1.5924	3.0	Hα	VVDS_LBT_OCT20_1d_178934_M11Hsky_S15
179071	36.3389785	−4.6466188	2.1121	4.0	Hα	VVDS_LBT_OCT20_1d_179071_M11Ksky_S18
179905	36.6104572	−4.6444695	2.0608	4.0	Hα	VVDS_LBT_OCT20_1d_179905_M8Ksky_S17
179905	36.6104572	−4.6444695	2.0601	4.0	Hα	VVDS_LBT_OCT20_1d_179905_M14Ksky_S11
179990	36.6410461	−4.6449848	2.0356	3.0	Hα	VVDS_LBT_OCT20_1d_179990_M8Ksky_S15
179990	36.6410461	−4.6449848	2.0356	3.0	Hα	VVDS_LBT_OCT20_1d_179990_M14Ksky_S14
180446	36.3482592	−4.6438773	1.5936	4.0	Hα	VVDS_LBT_OCT20_1d_180446_M11Hsky_S13
181261	36.6620577	−4.6416814	2.1613	3.0	Hα	VVDS_LBT_OCT20_1d_181261_M8Ksky_S12
182940	36.6496611	−4.6387972	1.4648	3.0	Hα	VVDS_LBT_OCT20_1d_182940_M8Hsky_S12
185040	36.6119311	−4.6349522	2.2231	4.0	Hα	VVDS_LBT_OCT20_1d_185040_M8Ksky_S16
185523	36.6239302	−4.6337579	2.0396	4.0	Hα	VVDS_LBT_OCT20_1d_185523_M14Ksky_S12

Table B.1. continued.

OBJ_ID	RA	Dec	z_{spec}	Flag	Line	1D-Spectum
364094	36.1562797	−4.3005582	1.6041	3.0	Hα	VVDS_LBT_OCT20_1d_364094_M12Hsky_S12
365897	36.1601525	−4.2975043	2.2641	3.5	Hα	VVDS_LBT_OCT20_1d_365897_M12Ksky_S13
369449	36.1630987	−4.2916442	2.1381	3.5	Hα	VVDS_LBT_OCT20_1d_369449_M12Ksky_S12
370077	36.1404797	−4.2901132	2.2831	3.0	Hα	VVDS_LBT_OCT20_1d_370077_M12Ksky_S14
373735	36.1359352	−4.2834295	2.3121	3.0	Hα	VVDS_LBT_OCT20_1d_373735_M12Ksky_S20
383107	36.1552194	−4.265314	2.1861	3.0	[O III]	VVDS_LBT_OCT20_1d_383107_M12Hsky_S19
383107	36.1552194	−4.265314	2.1861	3.0	Hα	VVDS_LBT_OCT20_1d_383107_M12Ksky_S19
384395	36.1729741	−4.2637323	1.5656	3.0	Hα	VVDS_LBT_OCT20_1d_384395_M12Hsky_S16
385771	36.1347704	−4.25996	1.5660	4.0	Hα	VVDS_LBT_OCT20_1d_385771_M12Hsky_S15
390991	36.134847	−4.2505199	1.7036	3.5	Hα	VVDS_LBT_OCT20_1d_390991_M12Hsky_S14
395770	36.1589829	−4.2421372	2.0961	3.0	Hα	VVDS_LBT_OCT20_1d_395770_M12Ksky_S16
433842	36.3966135	−4.1783018	2.1341	3.5	Hα	VVDS_LBT_OCT20_1d_433842_M10Ksky_S18
434177	36.378452	−4.1779649	1.6138	3.0	Hα	VVDS_LBT_OCT20_1d_434177_M10Hsky_S11
437678	36.4035061	−4.1727462	2.2566	4.0	Hα	VVDS_LBT_OCT20_1d_437678_M10Ksky_S17
439294	36.3874695	−4.1691679	1.6311	3.0	Hα	VVDS_LBT_OCT20_1d_439294_M10Hsky_S12
444135	36.3733867	−4.1615026	2.1692	3.5	Hα	VVDS_LBT_OCT20_1d_444135_M10Ksky_S16
446244	36.4085951	−4.1577974	1.5561	4.0	Hα	VVDS_LBT_OCT20_1d_446244_M10Hsky_S13
447002	36.4085929	−4.1569321	1.5541	3.0	Hα	VVDS_LBT_OCT20_1d_447002_M10Hsky_S13
511951	36.2024782	−4.0510283	1.4936	4.0	Hα	VVDS_LBT_OCT20_1d_511951_M7Hsky_S14
513770	36.1631932	−4.0473276	2.1621	3.5	Hα	VVDS_LBT_OCT20_1d_513770_M7Ksky_S15
515718	36.1910121	−4.043192	2.3256	3.0	[O III]	VVDS_LBT_OCT20_1d_515718_M7Hsky_S23
515718	36.1910121	−4.043192	2.3261	3.0	Hα	VVDS_LBT_OCT20_1d_515718_M7Ksky_S16
523367	36.2055719	−4.0311235	1.6041	3.5	Hα	VVDS_LBT_OCT20_1d_523367_M7Hsky_S15
527425	36.1997576	−4.0239239	2.2281	3.0	Hα	VVDS_LBT_OCT20_1d_527425_M7Ksky_S13
540741	36.1744902	−4.0002201	2.2516	4.0	Hα	VVDS_LBT_OCT20_1d_540741_M7Ksky_S23
542094	36.1703008	−4.0064452	1.6061	4.0	Hα	VVDS_LBT_OCT20_1d_542094_M7Hsky_S11